

Super-heterodyne light scattering on interacting colloidal suspensions: theory and experiment

Thomas Palberg, Holger Reiber, Tetyana Köller

Johannes Gutenberg Universität, Institut für Physik,

Staudingerweg 7, D-55128 Mainz, Germany

Martin Medebach

Technische Universität Berlin, Ivan-N.-Stranski Laboratory,

Strasse des 17. Juni 135, D-10623 Berlin, Germany

Gerhard Nägele

Forschungszentrum Jülich GmbH, IFF, D-52425 Jülich, Germany

(Dated: November 1, 2018)

In soft matter structure couples to flow and vice versa. Complementary to structural investigations, we here are interested in the determination of particle velocities of charged colloidal suspensions of different structure under flow. In a combined effort of theory and experiment we determine the Fourier transform of the super-heterodyne field autocorrelation function (power spectrum) which in frequency space is found to be well separated from homodyne contributions and low frequency noise. Under certain conditions the power spectrum is dominated by incoherently scattered light, originating from the unavoidable size polydispersity of colloidal particles. A simple approximate form for the low-wavenumber self-intermediate scattering function is proposed, reminiscent to the case of non-interacting particles. We experimentally scrutinize the range of applicability of these simplified calculations on employing a parabolic electro-osmotic flow profile. Both for non-interacting and strongly interacting fluid particle systems, the spectra are well described as diffusion-broadened velocity distributions comprising an osmotic flow-averaged superposition of Lorentzians at distinct locations. We discuss the performance and scope of this approach with particular focus on moderately strong interactions and on multiphase flow. In addition, we point to some remaining theoretical challenges in connection to the observed linear increase of the effective diffusion constant and the integrated spectral power with increasing electric field strength.

I. INTRODUCTION

Soft condensed matter is typically characterized both by its softness and an internal structure on a mesoscopic scale. This allows convenient optical access to system structure and dynamics in equilibrium. Structural properties, obtained from static light scattering with good statistical accuracy can be compared to theoretical expectations and/or computer simulations [1, 2, 3]. In particular for systems of strongly interacting particles, local and global changes of structure and even phase transitions are frequently observed with and without flow, thus providing an interesting field for studies of non-equilibrium phenomena [4, 5, 6, 7, 8, 9, 10]. We are interested here with the complementary task of determining the (local) particle velocities in systems of interacting particles in arbitrary flow profiles (plate-plate or cone plate shear, Hagen-Poiseuille flow, electrophoretic-electro-osmotic flow in closed cells, thermophoresis, sedimentation etc.) and different structure (unstructured, fluid, crystalline) The combination of structure and flow measurements in suitable model systems should in the long run help to elucidate the fundamental coupling between both.

A well developed arsenal of methods is available to study the flow behavior of fluids in general. Quite frequently tracer particles are used [11]. Direct particle imaging nowadays is capable of fast scans of 3D velocity distributions, e.g., in gas turbulence [12] or wide field scans with high spatial resolution [13] (in particular holographic image velocimetry displays diffraction limited spatial resolution [11, 14]). Both imaging applications, however, often require a complex instrumentation, even if for 2D scans the less demanding speckle imaging velocimetry can be used [15]. Tracer experiments have also been reported on suspensions of interacting particles, but in general the choice of suitable systems is strongly restricted [16]. Laser Doppler velocimetry (LDV) on the other hand, which is a heterodyne light scattering technique, can be directly employed with pure samples and small particle sizes. LDV uses either real fringe or reference beam realizations [17]. Using fringe techniques, two laser beams are crossed in the sample cell to produce a local illuminating grating. For sufficiently dilute suspensions the particle motion can then be traced via an oscillating scattered intensity of frequency proportional to the particle velocity. For large particle concentrations the analysis of the scattered intensity yields the heterodyne intensity autocorrelation function (IACF) or its Fourier transform, the power spectrum. Contributions of low frequency noise and the homodyne IACF (stemming from the self beat of photons scattered off the

sample) as well as the overlap of the two Fourier transform components of the heterodyne IACF [18] (observed for low velocities) can be avoided by introducing a frequency shift between the two illuminating beams. Frequency shifting was first used for electrokinetic applications by Schätzel et al. to locally separate the diffusion and the small drift velocities in non-interacting particle systems [19]. It may be noted that in that work also an alternative data analysis was employed to obtain the so-called amplitude weighted phase structure function from the phase of the scattered light [20]. The main general drawback of fringe techniques however is their strictly local velocity detection implying a tedious point-by-point determination of the actual flow pattern [21].

By contrast in a reference beam set-up, a small portion of the illuminating beam is separated. It is re-combined at the detector place with the Doppler-shifted light scattered off a small volume of the sample to act there as local oscillator and give rise to beats in the detected intensity [22, 23, 24]. The beat frequency is proportional to the Doppler frequency and therefore can be analyzed by considering either the IACF or its Fourier transform pair, the power spectrum. As the illuminating beam crosses the complete sample cell (integral measurement [18]), in principle one obtains information on the velocity distribution in a non-interacting sample, provided the scattering particles are homogeneously distributed and all of same scattering power. Then the amplitude of the spectrum contains information on the number of scatterers moving with a given velocity, and for a known sample cell geometry the flow profile can be quantified.

The situation of interacting samples, where a locally different structure will lead to different amplitudes has not been rigorously treated. The present paper will make a first step in that direction. Further, in previous studies, the reference beam setup suffered from the restriction that the homodyne contribution centered around zero frequency could possibly overlap with the heterodyne scattering contribution containing the information on the particle velocities. In the present work, we use a straightforward extension of the approach, used by Schätzel et al. for fringe techniques, to integral reference beam techniques by introducing a frequency shift between illuminating and reference beam. This shift is also accounted for by us in the calculation and analysis of the super-heterodyne signal. The general theory of dynamic light scattering from colloidal particles is known since many years and has been summarized, e.g., in [22, 23, 25]. The heterodyne (electrophoretic) light scattering technique for dilute systems of non-interacting particles has been discussed thoroughly in [24]. The shifting method has been very shortly discussed in [26]. The present paper gives a theoretical derivation of the super-heterodyne intensity autocorrelation function and its Fourier-transform pair, the power spectrum.

Moreover, this derivation for the first time includes an account of the unavoidable polydispersity actually leading to a principal possibility to deal with differently structured systems. To be specific, the theoretical analysis of the super-heterodyne IACF reveals that the shape of the measured power spectrum is usually connected to a convolution of the particle velocity distribution and the microstructure of particles, since the heterodyne part of the IACF contains an amplitude factor related to the local 'static' structure factor. Thus, for suspensions of correlated particles, the assumption of a homogeneous distribution of scattering power may be invalidated if the microstructure of the system changes locally. It is a main point of the present paper to experimentally realize the solution to this problem as suggested by theory. Exploiting the dominance of incoherently scattered light at low scattering angles and strong particle interactions, we show that the spectra obtained from electro-osmotically sheared suspensions of fluid-like order still can be unequivocally interpreted as velocity distributions.

In addition we also observe an increase of the effective diffusion coefficient and the integrated spectral power with the electric field for the case of suspensions of interacting particles. The field-dependence of both quantities is approximately linear in the case of fluid-ordered systems under stationary flow, but more complex in the case colloidal crystals. Interestingly, the integrated power stays constant during shear-induced melting at constant applied field, suggesting that the additional spectral power is not induced by the structural change.

While the physics behind these two effects are not yet fully understood, our tests clearly show that we have a versatile tool for quantifying the flow behavior in the fluid-ordered state, and for qualitatively complementing structural measurements in the crystalline state and in multi-phase flow. Given this, our approach should have several interesting applications. First, it could be quite useful to characterize deviations from simple Hagen-Poiseuille flow in non-Newtonian fluids [4, 5, 6, 7, 8, 9, 10, 20, 27, 28, 29]. From a comparison of experimental results, it could be useful to separate the effects of shear, absolute drift velocity against the solvent and external fields on the suspension dynamics, thus enabling an extension of presently available theoretical approaches, e.g., to investigations on the dynamic structure factor for interacting suspensions under flow [23]. Our method should be also well suited to study laning effects occurring in mixtures with different particle speeds [30]. And finally, it has already turned out to be useful for quantitative electrophoresis experiments in interacting suspensions [31, 32, 33, 34, 35].

In what follows, we shall first explain the experimental set-up for integral super-heterodyne light scattering in the reference beam mode, then give a thorough derivation of the IACF and the

power spectrum for moderately polydisperse and strongly interacting charged-sphere suspensions. We then show that the assumptions made in our theoretical derivations can be well met in a typical experiment and verify the theoretical results with experiments on different experimental situations. We finally discuss the performance and scope of the super-heterodyne velocimetry method and give an outlook on open theoretical and experimental issues.

II. EXPERIMENTAL

A. Integral Super-heterodyne dynamic light scattering set-up

Colloidal particle velocities have been obtained from a home-built super-heterodyne reference beam mode Laser Doppler velocimetry setup. Our instrument is a consequent extension of the heterodyne reference beam technique presented previously [18], but in contrast to the latter contains a frequency shift between illuminating beam and reference beam. This ensures excellent discrimination of the electrophoretic signal from all other spectral components and low-frequency electronic noise. The set-up is shown schematically in Fig. 1. The beam of a Nd-Yag laser (L , $\lambda_0 = 532$ nm) of circular frequency $\omega_0 \sim 10^{15}$ Hz is split into two beams, a reference beam (r) and an illuminating beam (i), using a beam splitter. Alternatively also a sinusoidal transmission grid (G) can be used (Sine Patterns, Pittsford NY). The two beams are made parallel by a lens L_1 and each beam passes through a Bragg cell (BC) and is frequency shifted by the circular frequencies $\omega_i = 1.002$ MHz and $\omega_r = 1$ MHz, respectively, with a positive relative Bragg shift, $\Delta\omega_B = \omega_i - \omega_r > 0$, in the circular frequency corresponding to $\Delta f_B = \Delta\omega_B/2\pi = (2000 \pm 5)$ Hz. The larger frequency is realized for the illumination beam. The beams are redirected into the sample cell (S) by lens L_2 where they cross in suspension under an angle of $\Theta = 18.82$.

In addition to a polarizer (P) the detector side optics include a a set of apertures (A) to define the observed sample volume and an optical fibre to define the scattering vector \mathbf{q} . The scattering vector is

$$\mathbf{q} = \mathbf{k}_i - \mathbf{k}_s \quad (1)$$

where \mathbf{k}_i and \mathbf{k}_s are the wave vectors of the illuminating and scattered, respectively (c.f., Fig. 1). The modulus of the scattering vector is given as $q = (4\pi\nu_s/\lambda_0) \sin(\Theta/2) = 5.0 \mu\text{m}^{-1}$, where ν_s the index of refraction of the solvent. For the present sign convention, \mathbf{q} is proportional to the momentum transfer from the photon to the scattering particle. For so-called integral measurements,

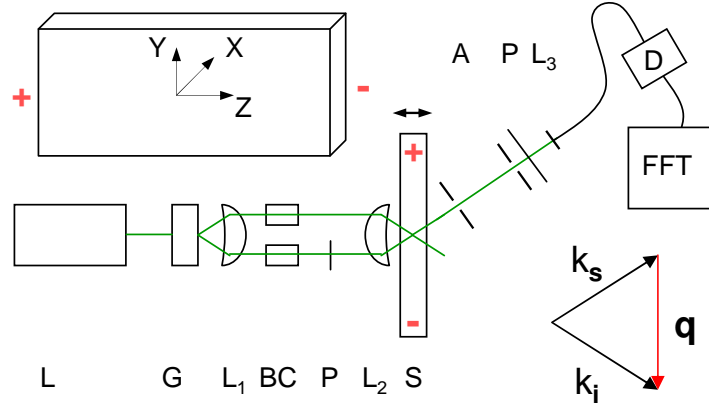


FIG. 1: Super-heterodyne velocimetry set-up. Top: Sketch of the rectangular flow-through cell and the used coordinate system. The plus and minus signs indicate the electrodes used to induce the combined electrophoretic-electro-osmotic flow. Middle: Top view of the super-heterodyne experiment (for a detailed description see text). Bottom right: definition of the scattering wave vector \mathbf{q} .

light scattered off the illuminated part of the sample is received within the acceptance angle of a grin lens. This lens is mounted at the inlet of an optical fibre leading to a photomultiplier used to record the intensity (D). Note that for the present definition of \mathbf{q} , the light scattered by a particle j moving with a velocity \mathbf{v}_j is Doppler-shifted by the circular frequency $\omega_D = -\mathbf{q} \cdot \mathbf{v}_j(x, y)$, where the velocity could be a function of the position. The frequency shift ω_D is positive, if the particle velocity shares an obtuse angle with the scattering vector $\mathbf{q} = q \hat{\mathbf{z}}$, where $\hat{\mathbf{z}}$ is the unit vector in z -direction. For example, in Fig. 1 a positive Doppler shift corresponds to particles moving towards the detector. Also the reference beam is directed into the fibre and superimposed with the scattered light. It therefore acts as a local oscillator, and gives rise to beats in the observed intensity which are analyzed by a Fast Fourier Transform analyzer (Ono Sokki DS2000, Compuress, Germany) to yield the power spectrum as a function of frequency $f = \omega/2\pi$. As we will discuss, the spectrum is composed of a strong peak at zero frequency, a homodyne term stemming from the self-beating of the scattered light, which is localized around zero frequency, and a super-heterodyne part, which is Doppler-shifted relative to the Bragg frequency shift Δf_B . The latter term contains all the information on particle velocity and direction and is further evaluated.

In our measurements, we have opted for a parabolic solvent flow profile. Such a profile can

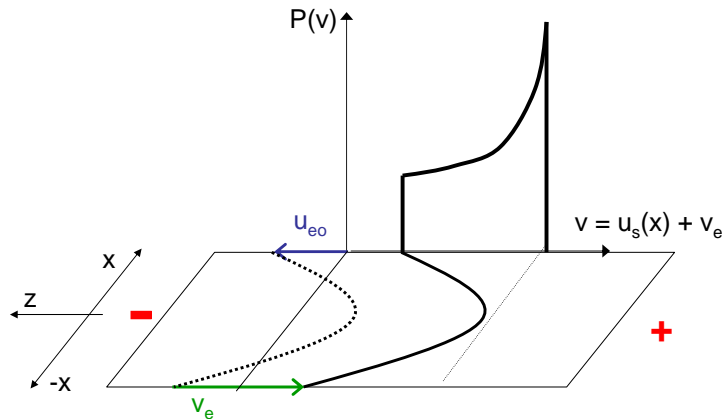


FIG. 2: Horizontal $x - z$ midplane: laboratory-frame velocity profiles $v(x) = v(x, y = 0)$ and $u_S(x) = u_S(x, y = 0)$ of particles and solvent, respectively. Vertical plane: corresponding probability density, $P(v)$, of finding a particle of given velocity v . In our setup, the external field \mathbf{E} , \mathbf{u}_{eo} and \mathbf{q} are aligned with the positive z -axis, whereas \mathbf{v}_e points into the negative z -direction.

be easily realized in a cylindrical tube, through which a suspension flows under a hydrostatic pressure difference. For strongly interacting suspensions, however, this approach often suffers from an insufficient stationarity of the flow, and an only moderate reproducibility [29]. Therefore, in the experiments discussed here, we have applied an electric field to move the particles and shear the suspension. Application of an external static electric field, \mathbf{E} , pointing into the positive z -axis in a closed cell geometry (see Fig. 1) allows for the development of an electro-osmotic flow profile of the incompressible solvent. Surface-released cations in the thin double layer at the negatively charged cell walls move towards the negative electrode with a velocity $u_{eo} > 0$ pointing along the positive z -axis (see Fig. 1) and drag some solvent along with them. A central solvent backflow in direction of the negative z -axis assures volume conservation of the incompressible fluid (Fig. 2). For DC electric fields a stationary parabolic flow profile results in both cylindrical geometry and the mid-plane of a rectangular cell [36]. For optical reasons we here employ a rectangular cell as shown with its electrodes in Fig. 1. The electro-osmotic flow profile, $u_S(x)$, of the solvent is sketched in Fig. 2 for the $x - z$ mid-plane located mid-cell of the rectangular cell at $y = 0$. Note that $u_S(x)$ is equal to u_{eo} at the side walls, and due to the rectangular cell shape, the integral of $u_S(x)$ with respect to x from one side wall to the other is zero due to volume conservation of the incompressible solvent.

Superimposed on this solvent flow profile is the electrophoretic motion of charged colloidal

particles relative to the solvent with the electrophoretic velocity $v_e = \mu_e E$, where μ_e is the electrophoretic mobility. The constant electrophoretic velocity $v_e < 0$ of the negatively charged colloids points in negative z direction towards the positive electrode. The resulting flow profile,

$$v(x) = v_e + u_S(x), \quad (2)$$

of colloidal particles in the laboratory frame is thus equal to the solvent profile shifted by the constant amount $|v_e|$ in negative z direction. Also drawn schematically in the Fig. 2 is the particle velocity distribution, $P(v)$, where $P(v) dv$ is the fraction of colloids with velocity in a infinitesimal interval dv around v . On assuming a homogeneous distribution of colloidal particles that remains unperturbed by the electro-osmotic flow, $P(v) \propto dx/dv$ [18].

Clearly the suspension is sheared at locally different rates by the underlying solvent flow. All colloidal particles and their electric double layers are subjected to the homogeneous electric field that couples differently to colloids and microions. If instead shear motion is introduced by a hydrostatic pressure difference and not by an electric field, the microions and the colloids are affected in the same way by the flow. If sedimentation is addressed in place of electrophoresis, gravity couples to the colloidal particles but not to the microions in the double layers and the solvent flow in sedimentation is not parabolic. Pipe flows are just one example of many possible shear profiles. For interacting colloidal particles, shear flow may lead to local phase transitions and, in concert with hydrodynamic interactions (HI), to a non-Newtonian flow behavior. This has been observed for both pressure and electro-kinetically driven flows [4, 5, 6, 7, 8, 21, 28, 29, 31, 32, 33, 34]. A fascinating richness of structural effects was there observed ranging from (partial) shear melting, to shear banding and shear induced structure formation, which all coupled back to the flow properties. In practically all cases deviations from the parabolic flow profile were observed. For the present paper we concentrate on one-phase systems of more or less pronounced fluid-like order and only shortly strive suspension flows with phase transitions. Consequently the theoretical section III is concerned with the derivation of the IACF and the corresponding superheterodyne spectrum for homogeneous systems in a stationary state.

B. Samples and sample preparation

One species of colloidal particles employed in this work are silica spheres synthesized by a modified Stöber synthesis, showing a diameter of $2a = 251$ nm and a relative standard deviation

in the size distribution of $s = 0.08$ determined from TEM-measurements. A representative TEM image is shown in the insert of Fig. 3. Suspensions of Si251 particles could be used in our measurements only in the fluid-like phase. Working at larger particle concentrations was inhibited by the onset of strong multiple scattering. The second species of spherical particles we have made use of is an industrial sample of Poly-n-Butylacrylamide-Polystyrene copolymer and a kind gift of BASF, Ludwigshafen. The PnBAPS68 particles have a diameter of $2a = 68$ nm and a standard deviation of $s = 0.05$ (determined from ultracentrifugation) and carry an effective charge of $Z = 420 e^-$ obtained from conductance measurements. The particle size distribution deduced from ultracentrifugation is shown in Fig. 3. Aqueous suspensions of this species can be investigated up to large particle concentrations without too much multiple scattering, so that we have studied them also in the crystalline state.

Both particle systems were prepared from pre-cleaned stock suspensions of large particle concentration stored over a mixed-bed ion exchanger. By precise dilution with milli-q-grade water, and by determining the particle density, n , using static light scattering, the desired number densities have been adjusted and the resulting suspensions filled in a closed Teflon-tubing circuit connecting an ion exchange chamber, a reservoir under an inert Ar atmosphere (to add further suspension, salt or solvent), and a set of different measurement cells. These comprised a conductivity experiment, a cell for static light scattering, and the flow-through cell for the velocity measurements. Details of the used preparation circle are given elsewhere [37, 38]. We here only

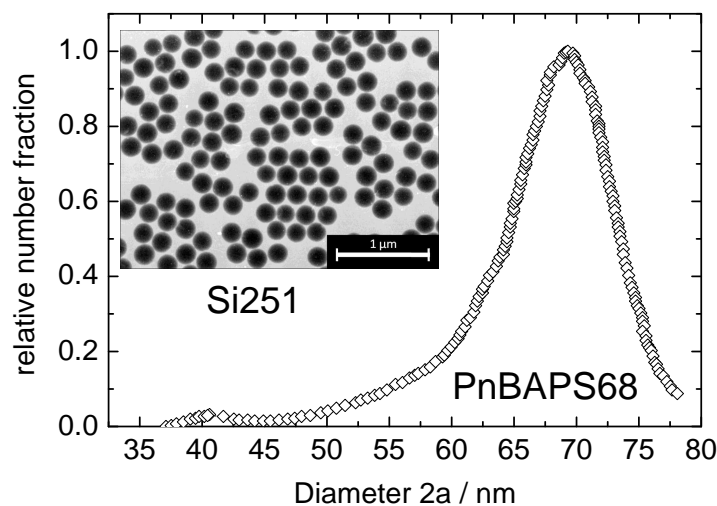


FIG. 3: Particle size distribution from ultracentrifugation for PnBAPS68. The insert shows a TEM picture of Si251. The scale bar is $1 \mu\text{m}$.

note that residual impurity concentrations on the level of the self-dissociation product of water are reached within a few hours. For measurements at elevated salt concentrations, *NaCl* solution was added after complete deionization. Continued cycling under bypassing the ion exchange column ensured homogenization, on controlling the salt concentration by conductivity measurements [39] and the particle concentration by static light scattering with a residual uncertainty of about one percent. This preparation method is thus very fast and assures good reproducibility of adjusted suspension parameters. Furthermore, the preparation circuit permits to conduct several experiments simultaneously. This is of great importance to have a continuous control on the constancy of interaction parameters.

C. Electrokinetic flow experiment

Electrophoretic-electro-osmotic shear flow experiments were performed in closed quartz cells of rectangular cross section with depth \times height $= d \times h = 1 \text{ mm} \times 10 \text{ mm}$ (Rank Bros. Bottisham Cambridge, UK). As sketched in Fig. 1 on the upper left, the origin of our coordinate system is at the cell center with $x \parallel d, y \parallel h$ and $z \parallel l$. The optical part of the cell length, l , spans some 40 mm and the effective platinum electrode distance is $l = 85.5 \text{ mm}$ as determined from calibration with an electrolyte dilution series. During the measurements the electrode chambers are sealed against the remaining preparation circuit by electromagnetic valves closed upon stop of pumping. To avoid accumulation of particles at the electrodes alternating square-wave fields of strength up to $E_{max} = U/l = 80 \text{ V/cm}$ were applied to fluid ordered systems. To ensure fully developed stationary flows, field switching frequencies $f_{AC} = (0.05 - 0.2) \text{ Hz}$ were used. Measurement intervals were restricted to one field direction, starting 2s after field reversal and ending 1s before the next field reversal.

III. THEORY

In this section we give the essentials of the theory of super-heterodyne electrophoretic light scattering from suspensions of charge-stabilized colloidal spheres subject to a constant external electric field. We proceed from non-interacting particles to low-salinity suspensions of strongly interacting particles. To our knowledge, the super-heterodyne electrophoretic scattering theory for strongly interacting colloidal particles has not been presented so far.

For a stationary and spatially homogeneous system, we derive the general expression for the measured intensity autocorrelation function (IACF) and its related power spectrum (PS) in terms of (partial) dynamic structure factors. The structure factors characterize the density fluctuation correlations of colloidal spheres in the presence of an external electric field. It will be discussed on how the electrophoretic velocity of the spheres may be deduced from small wave number measurements on weakly polydisperse systems.

A. Super-heterodyne scattering theory

The super-heterodyne scattering setup has been shown schematically in Fig. 1. We assume in the following that the colloidal spheres are optically isotropic, and that the Rayleigh-Gans-Debye description of weakly scattering particles applies where the electric fields scattered at each point inside a sphere can be linearly superimposed. The following general discussion does not include electro-osmotic flow effects which are of importance in closed cell geometries. The influence of a non-zero macroscopic solvent flow profile on the measured super-heterodyne power spectrum will be discussed in subsection III F.

Let the Bragg-shifted illuminating electric field be a plane wave of the form

$$\mathbf{E}_i(\mathbf{r}, \tau) = \hat{\mathbf{n}}_i E_i^0 \exp\{i(\mathbf{k}_i \cdot \mathbf{r} - [\omega_0 + \omega_i] \tau)\}, \quad (3)$$

where $\hat{\mathbf{n}}_i$ is the unit polarization vector of the incident field. Under the assumptions made above, and for the standard V-V geometry of polarized scattering, the field strength, $E_s(\mathbf{q}, \tau)$, of single-scattered light from N spheres in the scattering volume follows from standard scattering theory as [22, 23, 40]

$$E_s(\mathbf{q}, \tau) = \exp\{-i(\omega_0 + \omega_i) \tau\} c \sum_{l=1}^N f_l(q) \exp\{i\mathbf{q} \cdot \mathbf{r}_l(\tau)\}, \quad (4)$$

with \mathbf{q} as defined in Eq. (1). Here, $f_l(q)$, is the scattering amplitude of a sphere labelled by l , whose center at time τ is at the position $\mathbf{r}_l(\tau)$. For a homogeneous sphere of radius a_l , volume V_l and refractive index ν_l , the scattering amplitude is given by $f_l(q) = 2(\nu_l - \nu_s) V_l b_l(q) / \nu_s$, with the form amplitude $b_l(q) = 3j_1(qa_l) / (qa_l)$, where j_1 is the spherical Bessel function of first order. The apporative constant

$$c = E_i^0 \frac{\exp\{i|\mathbf{k}_s| R\}}{\lambda^2 R} \quad (5)$$

depends on λ , k_s , the large sample-to-detector distance R , and the field amplitude, E_i^0 , of the illuminating light [22, 23]. Its explicit form is of no concern, constant throughout the experiments

and thus will not be displayed any more. The corresponding electric field strength of the reference beam at the detector is

$$E_r(\tau) = E_r^0 \exp\{-i(\omega_0 + \omega_r)\tau\}. \quad (6)$$

The reference field is independent of the scattering wave vector and the particle configuration.

In the (super-)heterodyne setup, the intensity autocorrelation function of the mixed electric fields is analyzed by a real-time auto-correlator. For a stationary system, the super-heterodyne mixed-field intensity autocorrelation function (IACF) is given by

$$C_{\text{shet}}(\mathbf{q}, \tau) = \langle |E_s(\mathbf{q}, \tau) + E_r(\tau)|^2 \cdot |E_s(\mathbf{q}, 0) + E_r(0)|^2 \rangle, \quad (7)$$

where τ is the correlation time, which in our experiments is 10 – 100 ms or larger. The angular brackets denote a time average or likewise, for a stationary and ergodic system, an ensemble average. The IACF depends on the orientation of \mathbf{q} , since spatial isotropy is broken by the applied electric field. Carrying out the multiplications gives sixteen terms, ten of which vanish due to the assumed spatial homogeneity, and three of which are time-independent. The remaining three terms determine the time dependence of the IACF. To see this, we rewrite Eq. (7) as

$$C_{\text{shet}}(\mathbf{q}, \tau) = \langle [I_s(\mathbf{q}, \tau) + I_r(\tau) + E_r(\tau)E_s^*(\mathbf{q}, \tau) + E_r^*(\tau)E_s(\mathbf{q}, \tau)] \times \\ [I_s(\mathbf{q}, 0) + I_r(0) + E_r(0)E_s^*(\mathbf{q}, 0) + E_r^*(0)E_s(\mathbf{q}, 0)] \rangle, \quad (8)$$

with $I_s(\mathbf{q}, \tau) = E_s^*(\mathbf{q}, \tau) \cdot E_s(\mathbf{q}, \tau)$ and $I_r(\tau) = E_r^*(\tau) \cdot E_r(\tau)$. The asterisk denotes the operation of complex conjugation. The reference beam quantities, I_r and E_r , are independent of the ensemble average over the particle configurations. Moreover, the averages over products of an odd number of factors $E_s(\mathbf{q})$ and/or $E_s^*(\mathbf{q})$ vanish for $q > 0$, since spatial homogeneity requires the wave vector sum to be zero. For the same reason, $\langle E_s(\mathbf{q}, \tau)E_s(\mathbf{q}, 0) \rangle$ and $\langle E_s^*(\mathbf{q}, \tau)E_s^*(\mathbf{q}, 0) \rangle$ are identically zero. Using these properties of spatial homogeneity, we multiply the first element, $I_s(\mathbf{q}, \tau)$, in the upper bracket of Eq. (8) with the elements of the lower bracket, keeping terms only which are non-zero after averaging. On repeating this multiplication for the remaining three elements in the upper bracket, we obtain the intermediate result

$$C_{\text{shet}}(\mathbf{q}, \tau) = I_r [I_r + 2 \langle I_s(\mathbf{q}) \rangle] + 2 \text{Re} \{ E_r^*(\tau) E_r(0) \langle E_s(\mathbf{q}, \tau) \cdot E_s^*(\mathbf{q}, 0) \rangle \} + \\ \langle |E_s(\mathbf{q}, \tau)|^2 \cdot |E_s(\mathbf{q}, 0)|^2 \rangle, \quad (9)$$

showing that three out of six non-zero terms are time-independent, and add up to a constant baseline $I_r [I_r + 2 \langle I_s(\mathbf{q}) \rangle]$, where $I_r = |E_r^0|^2$ and $I_s(\mathbf{q}) = |E_s(\mathbf{q}, 0)|^2$. To make the frequency depen-

dence of $C_{\text{shet}}(\mathbf{q}, \tau)$ explicit, we redefine $E_s(\mathbf{q}, \tau)$ now as

$$E_s(\mathbf{q}, \tau) = c \sum_{l=1}^N f_l(q) \exp\{i\mathbf{q} \cdot \mathbf{r}_l(\tau)\}. \quad (10)$$

With this redefinition, we obtain

$$C_{\text{shet}}(\mathbf{q}, \tau) = I_r [I_r + 2 \langle I_s(\mathbf{q}) \rangle] + 2 I_r \text{Re} [g_E(\mathbf{q}, \tau) \exp\{-i \Delta\omega_B \tau\}] + g_I(\mathbf{q}, \tau), \quad (11)$$

for the super-heterodyne scattering function, where $\Delta\omega_B = \omega_i - \omega_r > 0$. The standard expression for heterodyne scattering is recovered for zero Bragg shift [25]. Note that $C_{\text{shet}}(\mathbf{q}, \tau)$ does not depend on ω_0 since, due to the mixing of $E_s(\mathbf{q}, \tau)$ and $E_r^*(\tau)$, it only contains the low-frequency beats.

Information on the particle motion is embedded in the super-heterodyne part of the mixed-field IACF, given by the electric field-autocorrelation function (EACF) of the scattered light

$$g_E(\mathbf{q}, \tau) = \langle E_s(\mathbf{q}, \tau) \cdot E_s^*(\mathbf{q}, 0) \rangle. \quad (12)$$

The mixed-field IACF contains also a homodyne part, equal to the homodyne intensity autocorrelation function,

$$g_I(\mathbf{q}, \tau) = C_{\text{hom}}(\mathbf{q}, \tau) = \langle |E_s(\mathbf{q}, \tau)|^2 \cdot |E_s(\mathbf{q}, 0)|^2 \rangle \quad (13)$$

which is of order $\mathcal{O}(E_s^4)$. We further note that $g_E(\mathbf{q}, 0) = \langle I_s(\mathbf{q}) \rangle$, and $g_I(\mathbf{q}, 0) = \langle I_s^2(\mathbf{q}) \rangle$. In standard heterodyne experiments, $\langle I_s \rangle \ll I_r$, and the homodyne contribution is negligibly small. Eq. (11) reduces then to

$$C_{\text{shet}}(\mathbf{q}, \tau) = I_r^2 + 2 I_r \langle I_s(\mathbf{q}) \rangle (1 + \text{Re} [\widehat{g}_E(\mathbf{q}, \tau) \exp\{-i \Delta\omega_B \tau\}]), \quad (14)$$

with the normalized EACF of the scattered light,

$$\widehat{g}_E(\mathbf{q}, \tau) = \frac{g_E(\mathbf{q}, \tau)}{\langle I_s(\mathbf{q}) \rangle}, \quad (15)$$

defined such that $\widehat{g}_E(\mathbf{q}, 0) = 1$. The EACF is complex-valued for a non-isotropic system in an external field.

B. Scattered field with Gaussian statistics

So far, we have not assumed that the scattered field is a complex central Gaussian random variable, an assumption frequently made in dynamic light scattering theory. This assumption is

certainly valid for dilute suspensions with weak particle correlations, where it becomes a consequence of the central limit theorem. It is violated, however, in very dense suspensions of glass-like or gel-like character that show dynamic heterogeneity [41], and in live sperm cells. For a scattered field of Gaussian character, Eq. (11) can be derived alternatively using Wick's theorem for the average of products of central Gaussian random variables [23]. Another consequence of Wick's theorem is that for a Gaussian scattered field, $g_I(\mathbf{q}, \tau)$ includes no information on the suspension dynamics, not contained already in $g_E(\mathbf{q}, \tau)$, and that they are related by the Siegert relation

$$\widehat{g}_I(\mathbf{q}, \tau) = 1 + |\widehat{g}_E(\mathbf{q}, \tau)|^2, \quad (16)$$

with $\widehat{g}_I(\mathbf{q}, 0) = 2$. The mixed-field IACF for a scattered field of Gaussian statistics is thus

$$\begin{aligned} C_{\text{shet}}(\mathbf{q}, \tau) &= [I_r + \langle I_s(\mathbf{q}) \rangle]^2 + 2I_r \langle I_s(\mathbf{q}) \rangle \text{Re} [\widehat{g}_E(\mathbf{q}, \tau) \exp\{-i \Delta\omega_B \tau\}] \\ &\quad + \langle I_s(\mathbf{q}) \rangle^2 |\widehat{g}_E(\mathbf{q}, \tau)|^2 \end{aligned} \quad (17)$$

with the normalized scattered-field IACF,

$$\widehat{g}_I(\mathbf{q}, \tau) = \frac{g_I(\mathbf{q}, \tau)}{\langle I_s(\mathbf{q}) \rangle^2}, \quad (18)$$

defined such that $\widehat{g}_I(\mathbf{q}, 0) = \langle I_s^2(\mathbf{q}) \rangle / \langle I_s(\mathbf{q}) \rangle^2 \geq 1$. For a non-Gaussian scattered light field, however, one has to deal with two genuinely different correlation functions $g_E(\mathbf{q}, \tau)$ and $g_I(\mathbf{q}, \tau)$.

C. Super-heterodyne power spectrum

When a spectrum analyzer is used in place of a time correlator to analyze the superposition of scattered and reference light, the power spectrum is determined in place of the mixed-field IACF. The power spectrum is the temporal Fourier transform of the mixed-field IACF, namely

$$C_{\text{shet}}(\mathbf{q}, \omega) = \frac{1}{2\pi} \int_{-\infty}^{\infty} d\tau \exp\{i\omega\tau\} C_{\text{shet}}(\mathbf{q}, \tau) = \frac{1}{\pi} \int_0^{\infty} d\tau \cos\{\omega\tau\} C_{\text{shet}}(\mathbf{q}, \tau), \quad (19)$$

where the second equality follows from the stationarity property $C_{\text{shet}}(\mathbf{q}, \tau) = C_{\text{shet}}(\mathbf{q}, -\tau)$. Stationarity implies further that $g_E(\mathbf{q}, \tau) = g_E(\mathbf{q}, -\tau)^*$ and $g_I(\mathbf{q}, \tau) = g_I(\mathbf{q}, -\tau)$. The mixed-field IACF and its power spectrum are measurable quantities and therefore real-valued. The power spectrum is symmetric in ω , that is it consists of two sub-spectra extending symmetrically to positive and negative frequencies. Furthermore, it fulfills the sum rule

$$\int_{-\infty}^{\infty} d\omega C_{\text{shet}}(\mathbf{q}, \omega) = C_{\text{shet}}(\mathbf{q}, \tau = 0) = (I_r)^2 + 4I_r \langle I_s(\mathbf{q}) \rangle + \langle I_s(\mathbf{q}) \rangle^2. \quad (20)$$

The 'static' quantity $\langle I_s(\mathbf{q}) \rangle = \langle I_s(-\mathbf{q}) \rangle$ in a driven, non-equilibrium system still depends on the hydrodynamic interactions [42].

D. Non-interacting colloidal spheres

Consider a very dilute charge-stabilized suspension, which includes a sufficient amount of added salt ions, so that the colloidal spheres are non-interacting. Suppose that the N spheres in the scattering volume form m components, with N_α particles in component $\alpha \in \{1, \dots, m\}$. The position vectors of non-interacting spheres are independent so that

$$\langle I_s^o(\mathbf{q}) \rangle = |c|^2 \sum_{\alpha=1}^m N_\alpha f_\alpha^2(q), \quad (21)$$

and

$$\widehat{g}_E^o(\mathbf{q}, \tau) = \frac{\sum_{\alpha=1}^m x_\alpha f_\alpha^2(q) G_\alpha^o(\mathbf{q}, \tau)}{\sum_{\alpha=1}^m x_\alpha f_\alpha^2(q)}. \quad (22)$$

Here, $x_\alpha = N_\alpha/N$ is the molar fraction, $f_\alpha(q)$ the scattering amplitude, and

$$G_\alpha^o(\mathbf{q}, \tau) = \langle \exp\{i\mathbf{q} \cdot (\mathbf{r}_\alpha(\tau) - \mathbf{r}_\alpha(0))\} \rangle, \quad (23)$$

the self-intermediate scattering function of component α . The label (o) indicates properties of a system of non-interacting particles.

The self-intermediate scattering function is the spatial Fourier transform of the fundamental solution $P_s(\mathbf{r}, \tau | \mathbf{r}_0)$, with $P_s(\mathbf{r}, 0 | \mathbf{r}_0) = \delta(\mathbf{r} - \mathbf{r}_0)$, of the Smoluchowski equation,

$$\frac{\partial}{\partial \tau} P_s(\mathbf{r}, \tau) = D_0 \nabla^2 P_s(\mathbf{r}, \tau) - \mathbf{v}_e^o \cdot \nabla P_s(\mathbf{r}, \tau), \quad (24)$$

which is used to describe a single microion-dressed charged colloidal sphere of diffusion coefficient D_0 in an unbounded and quiescent fluid subject to a constant electric field \mathbf{E} . The colloidal macroion responds to this forcing by acquiring a terminal mean drift velocity relative to the quiescent solvent

$$\mathbf{v}_e^o = \mu_e^o \mathbf{E}, \quad (25)$$

once the polarization of the microionic electric double layers (EDL) in response to the external field has acquired a steady state after the relaxation time $\tau_{DL} = (\kappa^2 D_{el})^{-1}$, which is typically 10^{-7} s for a 1 mM electrolyte solution [43]. Here, μ_e^o is the electrophoretic mobility of a colloidal

macroion in isolation, and κ^{-1} and D_{el} are the Debye screening length and mean diffusion coefficient, respectively, of electrolyte ions. The assumption underlying the use of the forced diffusion Eq. (24) is that the particle diffusion and the electrokinetic effects on the EDL caused by the applied field are independent. This assumption is reasonable for a weak field which can be treated as a first-order perturbation (linear electrophoresis). The field-independent mobility of a spherical colloid can be calculated using standard electrokinetic mean-field theory (see, e.g., [43, 44]) or extensions which account for microion correlations [45]. These theories provide a relation between the experimentally determined electrophoretic mobility and the zeta potential or related electrophoretic colloid charge.

The fundamental solution of the single-colloid Smoluchowski equation is

$$P_s(\mathbf{r}, \tau \geq 0 | \mathbf{r}_0) = \frac{1}{(4\pi D_0 \tau)^{3/2}} \exp\left\{-\frac{[\mathbf{r} - \mathbf{r}_0 - \mathbf{v}_e^o \tau]^2}{4D_0 \tau}\right\}, \quad (26)$$

stating that $\mathbf{r} - \mathbf{r}_0 - \mathbf{v}_e^o \tau$ is a central Gaussian random variable so that $g_I^o(\mathbf{q}, \tau)$ is related to $g_E^o(\mathbf{q}, \tau)$ by the Siegert relation.

Eq. (26) applies also to a polydisperse system of statistically independent spheres of varying electrophoretic drift velocities. Electrophoresis differs from sedimentation in that the total force exerted on the suspension is zero due to overall electro-neutrality. This has consequences for the range of the HI, which is shorter in the case of electrophoresis [46, 47].

The self-intermediate scattering function of an isolated sphere of diffusion coefficient $D_0 = k_B T / (6\pi\eta_0 a)$, which drifts with the mean velocity $\mathbf{v}_e^o = \mu_e^o \mathbf{E}$, follows from Fourier-transforming the fundamental solution,

$$\begin{aligned} G^o(\mathbf{q}, \tau \geq 0) &= \int d(\mathbf{r} - \mathbf{r}_0) \exp\{i\mathbf{q} \cdot (\mathbf{r} - \mathbf{r}_0)\} P_s(\mathbf{r}, \tau | \mathbf{r}_0) \\ &= \exp\{i\mathbf{q} \cdot \mathbf{v}_e^o \tau\} \exp\{-q^2 D_0 \tau\}, \end{aligned} \quad (27)$$

where the sign convention in the Fourier transform has been made consistent with the one in Eq. (23).

In summary, the normalized EACF and IACF of a monodisperse suspension of non-interacting colloidal spheres with equal electrophoretic drift velocity \mathbf{v}_e^o is given, for all τ , by

$$\widehat{g}_E^o(\mathbf{q}, \tau) = \exp\{i\mathbf{q} \cdot \mathbf{v}_e^o \tau\} \exp\{-q^2 D_0 |\tau|\} \quad (28)$$

$$\widehat{g}_I^o(\mathbf{q}, \tau) = 1 + \exp\{-2q^2 D_0 |\tau|\}, \quad (29)$$

which shows that the homodyne part of the mixed-field IACF is independent of \mathbf{v}_e^o as long as no differential motion between two spheres due to different drift velocities occurs. Polydispersity in

the particle mobility would introduce such a differential motion between different components α and β and thus be detectable as an oscillation in $\widehat{g}_I^o(\mathbf{q}, \tau)$ [48]. Continuing with the case of equal drift velocities and using Eq. (17), the mixed-field IACF becomes

$$C_{\text{shet}}^o(\mathbf{q}, \tau) = [I_r + \langle I_s^o(\mathbf{q}) \rangle]^2 + 2I_r \langle I_s^o(\mathbf{q}) \rangle \cos [(\Delta\omega_B - \mathbf{q} \cdot \mathbf{v}_e^o) \tau] \exp\{-q^2 D_0 |\tau|\} + \langle I_s^o(\mathbf{q}) \rangle^2 \exp\{-2q^2 D_0 |\tau|\}, \quad (30)$$

where $I_s^o(\mathbf{q}) = |c|^2 N f^2(q)$. Suppose now that $\langle I_s^o \rangle \ll I_r$. Then,

$$C_{\text{shet}}^o(\mathbf{q}, \tau) = I_r^2 + 2I_r \langle I_s^o(\mathbf{q}) \rangle + 2I_r \langle I_s^o(\mathbf{q}) \rangle \cos [(\Delta\omega_B - \mathbf{q} \cdot \mathbf{v}_e^o) \tau] \exp\{-q^2 D_0 |\tau|\}, \quad (31)$$

i.e., provided the homodyne part is negligibly, $C_{\text{shet}}^o(\mathbf{q}, \tau)$ is an exponentially damped cosine in τ , shifted upward by a time-independent baseline, and characterized by a

$$\begin{aligned} \text{decay time: } \tau_q &= \frac{1}{q^2 D_0} \\ \text{period: } T &= \frac{2\pi}{|\Delta\omega_B - \mathbf{q} \cdot \mathbf{v}_e^o|}. \end{aligned} \quad (32)$$

Thus, a measurement of the mixed-field IACF provides a simultaneous determination of the diffusion coefficient and the electrophoretic mobility, given in our setup by $\mu_e^o = |(\mathbf{q} \cdot \mathbf{v}_e^o)|/(qE)$. Super-heterodyning using Bragg cells has two effects not present in a conventional heterodyne setup: First, through the appearance of a non-zero $\Delta\omega_B$, the oscillation period T can be shortened relative to the decay time τ_q , which allows for an improved resolution in v_e^o , and second, the method is sensitive to the sign of \mathbf{v}_e^o . A drift velocity parallel to $\mathbf{q} \parallel \mathbf{E} \parallel \widehat{\mathbf{z}}$ or, more generally, a velocity \mathbf{v}_e^o sharing an acute angle with \mathbf{q} , enlarges the period of oscillations, whereas antiparallel motion causes the period to decrease. In our setup, the negatively charged colloids move antiparallel to the \mathbf{q} -axis (i.e., $-\mathbf{q} \cdot \mathbf{v}_e^o = q|v_e^o| > 0$), so that a reduction in the period T is achieved. The resolution can be further improved by making τ_q larger, that is by choosing the scattering angle as small as possible. For typical colloids, $\tau_q^{-1} = \Delta\omega \sim 10^3$ Hz, so that the symmetric frequency broadening due to the isotropic diffusive motion of spheres is comparable to the frequency shift by the Bragg cells.

Using Eq. (19), the mixed-field power spectrum is obtained as

$$\begin{aligned} C_{\text{shet}}^o(\mathbf{q}, \omega) &= [I_r + \langle I_s^o(\mathbf{q}) \rangle]^2 \delta(\omega) \\ &+ \frac{I_r \langle I_s^o(\mathbf{q}) \rangle}{\pi} \left[\frac{q^2 D_0}{(\omega + [\Delta\omega_B - \mathbf{q} \cdot \mathbf{v}_e^o])^2 + (q^2 D_0)^2} + \frac{q^2 D_0}{(\omega - [\Delta\omega_B - \mathbf{q} \cdot \mathbf{v}_e^o])^2 + (q^2 D_0)^2} \right] \\ &+ \frac{\langle I_s^o(\mathbf{q}) \rangle^2}{\pi} \frac{2q^2 D_0}{\omega^2 + (2q^2 D_0)^2}. \end{aligned} \quad (33)$$

It is the sum of an irrelevant singular term at $\omega = 0$ due to the non-subtracted baseline contribution, and two symmetrically shifted Lorentzian curves of half-width at half-height $q^2 D_0$, centered at $\omega = \pm [\Delta\omega_B - \mathbf{q} \cdot \mathbf{v}_e^0]$, which is the interesting super-heterodyne part, and an unshifted Lorentzian of double-sized half-width at half-height $2q^2 D_0$, centered at $\omega = 0$. The last contribution is due to the self-beating of the scattered light (homodyne part) and contains no information on the electrophoretic motion. The two heterodyne Lorentzians are Bragg-shifted away from the origin by $\Delta\omega_B$, so that they can be better distinguished from the central homodyne Lorentzian. Since \mathbf{q} is parallel to $\mathbf{E} = E\hat{\mathbf{z}}$ in our setup, and since the negatively charged colloids move antiparallel to the field, the centers of the super-heterodyne Lorentzians are separated from the frequency origin by $\Delta\omega_B + q\mu_e^0 E$, so that this separation increases with increasing field strength. The frequency resolution improves with decreasing q and D_0 , and increasing field strength E . Note that the frequency shift in the mixed-field power spectrum corresponds to the sinusoidal modulation in the mixed-field EACF.

When the electrophoretic mobilities vary from particle to particle possibly due to some charge polydispersity, the super-heterodyne part of the mixed-field IACF in Eq. (11) is generalized to

$$C_{\text{shet}}^o(\mathbf{q}, \tau)|_{\text{part}} = 2I_r \langle I_s^o(\mathbf{q}) \rangle \text{Re} \left[\langle \hat{g}_E^o(\mathbf{q}, \tau) \rangle_{\mu_e} \exp\{-i\Delta\omega_B \tau\} \right], \quad (34)$$

where $\langle \dots \rangle_{\mu_e}$ denotes an average over the mobility distribution. A narrow distribution characterized by the mean mobility $\bar{\mu}_e$ and the relative standard deviation σ_{μ_e} , can be approximated by a Gaussian, yielding [48]

$$C_{\text{shet}}^o(\mathbf{q}, \tau)|_{\text{part}} = 2I_r \langle I_s^o(\mathbf{q}) \rangle \exp\left\{-q^2 \left[D_0 |\tau| + \frac{1}{2} (\bar{\mu}_e E \tau)^2 \sigma_{\mu_e}^2 \right]\right\} \cos[(\Delta\omega_B + q\bar{\mu}_e E) \tau], \quad (35)$$

for non-interacting colloidal spheres. Hence the super-heterodyne part of the IACF decays faster than exponentially with a rate that increases with increasing mobility polydispersity σ_{μ_e} . The corresponding power spectrum has a shape similar to a Lorentzian centered at $\Delta\omega_B + q\bar{\mu}_e E$, but is broadened symmetrically by an amount that increases with increasing σ_{μ_e} .

A remark on the sign convention for \mathbf{q} made in Eq. (1) is in order here. In fact, we could have equally well used the definition $\mathbf{q} = -(\mathbf{k}_i - \mathbf{k}_s)$ for the scattering wave vector, which amounts to replacing \mathbf{q} by $-\mathbf{q}$ in Eq. (4). The only consequence is that $g_E(\mathbf{q}, \tau)$ must be replaced by $g_E(-\mathbf{q}, \tau) = g_E(\mathbf{q}, \tau)^*$ in all the following expressions, on noting further that $g_I(-\mathbf{q}, \tau) = g_I(\mathbf{q}, \tau)$ and $\langle I_s(-\mathbf{q}) \rangle = \langle I_s(\mathbf{q}) \rangle$. For non-interacting particles, this leads to the replacement of $\Delta\omega_B - \mathbf{q} \cdot \mathbf{v}_e^0$ by $\Delta\omega_B + \mathbf{q} \cdot \mathbf{v}_e^0$ in Eqs. (30 - 33). This makes it obvious that the outcome of the experiment is independent on the sign convention used for the scattering vector.

E. Interacting colloidal spheres

Information on the colloid velocities is embodied only in the super-heterodyne part of $C_{\text{shet}}(\mathbf{q}, \tau)$ that involves $g_E(\mathbf{q}, \tau)$. The normalized EACF of light scattered from N interacting spheres is given by

$$\widehat{g}_E(\mathbf{q}, \tau) = \frac{\sum_{l,j=1}^N f_l(q) f_j(q) \langle \exp\{i\mathbf{q} \cdot [\mathbf{r}_l(\tau) - \mathbf{r}_j(0)]\} \rangle}{\sum_{l,j=1}^N f_l(q) f_j(q) \langle \exp\{i\mathbf{q} \cdot [\mathbf{r}_l - \mathbf{r}_j]\} \rangle}. \quad (36)$$

Consider first an ideally monodisperse suspension of identical spheres. Then,

$$\widehat{g}_E(\mathbf{q}, \tau) = \frac{S(\mathbf{q}, \tau)}{S(\mathbf{q})}, \quad (37)$$

and

$$\langle I_s(\mathbf{q}) \rangle = |c|^2 N f^2(q) S(\mathbf{q}). \quad (38)$$

Here,

$$S(\mathbf{q}, \tau) = \left\langle \frac{1}{N} \sum_{l,j=1}^N \exp\{i\mathbf{q} \cdot [\mathbf{r}_l(\tau) - \mathbf{r}_j(0)]\} \right\rangle \quad (39)$$

is the complex-valued, steady-state dynamic structure factor. The corresponding steady-state structure factor is $S(\mathbf{q}) = S(\mathbf{q}, 0)$.

For a m component mixture, it follows from Eq. (36) that

$$\widehat{g}_E(\mathbf{q}, \tau) = \frac{\sum_{\alpha,\beta=1}^m (x_\alpha x_\beta)^{1/2} f_\alpha(q) f_\beta(q) S_{\alpha\beta}(\mathbf{q}, \tau)}{\sum_{\alpha,\beta=1}^m (x_\alpha x_\beta)^{1/2} f_\alpha(q) f_\beta(q) S_{\alpha\beta}(\mathbf{q})}, \quad (40)$$

with the partial dynamic structure factor of $\alpha - \beta$ colloid pairs defined by

$$S_{\alpha\beta}(\mathbf{q}, \tau) = \left\langle \frac{1}{(N_\alpha N_\beta)^{1/2}} \sum_{l=1}^{N_\alpha} \sum_{j=1}^{N_\beta} \exp\left\{i\mathbf{q} \cdot \left[\mathbf{r}_l^\alpha(\tau) - \mathbf{r}_j^\beta(0)\right]\right\} \right\rangle, \quad (41)$$

where \mathbf{r}_l^α points to the center of a sphere l belonging to component α . The partial dynamic structure factor can be written as the sum of a self- and distinct part,

$$S_{\alpha\beta}(\mathbf{q}, \tau) = \delta_{\alpha\beta} G_\alpha(\mathbf{q}, \tau) + S_{\alpha\beta}^d(\mathbf{q}, \tau), \quad (42)$$

where the self-intermediate scattering function of an α -type sphere is defined such that $G_\alpha(\mathbf{q}, 0) =$

1. On invoking the definition

$$S_M(\mathbf{q}, \tau) = \frac{1}{f^2(q)} \sum_{\alpha,\beta=1}^m (x_\alpha x_\beta)^{1/2} f_\alpha(q) f_\beta(q) S_{\alpha\beta}(\mathbf{q}, \tau) \quad (43)$$

of the measurable dynamic structure factor in a polydisperse system, and

$$\overline{f^p}(q) = \sum_{\alpha=1}^m x_{\alpha} f_{\alpha}(q)^p, \quad (44)$$

for any integer p , Eq. (40) is rewritten in more compact notation as

$$\widehat{g}_E(\mathbf{q}, \tau) = \frac{S_M(\mathbf{q}, \tau)}{S_M(\mathbf{q})}, \quad (45)$$

with $S_M(\mathbf{q}) = S_M(\mathbf{q}, 0)$.

Suppose now that the m components differ only in their scattering amplitudes $\{f_{\alpha}(q)\}$, but are otherwise identical. For such an interaction-monodisperse system, the partial dynamic structure factors reduce to [2]

$$S_{\alpha\beta}(\mathbf{q}, \tau) = \delta_{\alpha\beta} G(\mathbf{q}, \tau) + (x_{\alpha} x_{\beta})^{1/2} [S(\mathbf{q}, \tau) - G(\mathbf{q}, \tau)], \quad (46)$$

where $G(\mathbf{q}, \tau)$ and $S(\mathbf{q}, \tau)$ are, respectively, the self-intermediate scattering function and the dynamic structure factor of an ideally monodisperse system. Therefore, for pure scattering polydispersity, the EACF of the scattered light reduces to

$$g_E(\mathbf{q}, \tau) = |c|^2 N \overline{f^2}(q) S_D(\mathbf{q}, \tau), \quad (47)$$

with the so-called decoupling (approximation) dynamic structure factor

$$S_D(\mathbf{q}, \tau) = X(q) G(\mathbf{q}, \tau) + [1 - X(q)] S(\mathbf{q}, \tau), \quad (48)$$

as an approximation to $S_M(\mathbf{q}, \tau)$, and the decoupling scattering factor

$$X(q) = 1 - \frac{\overline{f(q)}^2}{\overline{f^2(q)}}. \quad (49)$$

For a suspension of slightly size-polydisperse homogeneous spheres made of the same scattering material, $X(q)$ simplifies to

$$X(q) \approx 9s^2, \quad (50)$$

provided that $s < 0.1$ and $q\sigma < 1.5$, where $\sigma = 2a$ is the mean diameter. The polystyrene sphere samples explored in this work are only slightly size-polydisperse, characterized by the relative standard deviation of $s \approx 0.05$. For these systems, the assumption of interaction-monodispersity

is thus quite reasonable, and it implies for $9s^2 \ll 1$, and in the experimentally probed small- q range, that

$$g_E(\mathbf{q}, \tau) \approx |c|^2 N f^2(q) [9s^2 G(\mathbf{q}, \tau) + S(\mathbf{q}, \tau)] , \quad (51)$$

where terms of $O(s^4)$ and $O(s^2 \times S(\mathbf{q}))$ have been ignored. Here, $f(q)$ is the scattering amplitude of ideally monodisperse spheres of diameter σ .

For values of q well below the position, q_m , of the principal peak, the zero-field $S(q)$ of deionized suspensions is very small in comparison to one, since the osmotic compressibility is very low. In these deionized fluid systems, $q_m \approx 2\pi n^{1/3} = (6\pi^2 \phi)^{1/3} / a$, where ϕ is the volume fraction of spheres [49].

On assuming that $S(\mathbf{q})$ remains very small for $|\mathbf{q}| \ll q_m$, also in the presence of a weak external field, as it can be expected in the linear response regime, we obtain approximately

$$\hat{g}_E(\mathbf{q}, \tau) \approx G(\mathbf{q}, \tau) , \quad (52)$$

provided that $q \ll q_m$ and $S(\mathbf{q}) \ll 9s^2$. The scattered-field EACF in the super-heterodyne part of Eq. (11) is then determined essentially by the self-intermediate scattering function, without significant contributions from $S(\mathbf{q}, \tau)$.

We point out here that the field-free coherent scattering contribution, $S(q, \tau)$, to $S_D(q, \tau)$ decays faster than $G(q, \tau)$ at low q , even at longer times when the slowing influence of particle caging comes into play. This is due to the large value of the (field-free) collective diffusion coefficient, $D_c = D_0 H(q \rightarrow 0) / S(q \rightarrow 0)$ in comparison to D_0 , where $H(q)$ is the so-called hydrodynamic function [49]. In fact, $G(q \ll q_m, \tau) \approx \exp\{-q^2 W(\tau)\}$ decays slowly at small q since the particle mean-squared displacement, $W(\tau)$, has a long-time slope equal to the long-time self-diffusion coefficient, that is significantly smaller than D_0 . For an example, near the freezing transition, the long-time self-diffusion coefficient amounts to only about ten percent of D_0 . Therefore, $G(\mathbf{q}, \tau)$ is expected to dominate $S(\mathbf{q}, \tau)$ even in presence of a weak external field.

It is a difficult task to calculate the dynamic structure factor, $S(\mathbf{q}, \tau)$, of interacting macroions in the presence of an electric field since this quantity depends on all ionic degrees of freedom. In fact, to our knowledge, no general theoretical or simulation results are available to date for the dynamic structure factor of interacting charged colloids in an external electric field. Results are known only for very simplifying models of driven colloid systems. To give an example, the stationary dynamic structure factor of a homogeneous and ideally monodisperse suspension of slowly

sedimenting colloidal spheres where (quite unrealistically) hydrodynamic interactions have been ignored is given by $S(\mathbf{q}, \tau) = S_{\text{eq}}(q, \tau) \times \exp\{i \mathbf{q} \cdot \mathbf{V}_{\text{sed}} \tau\}$. Here, \mathbf{V}_{sed} is the sedimentation velocity measured in the laboratory frame, which is corrected for the solvent backflow originating from the presence of the container bottom, and $S_{\text{eq}}(q, \tau)$ is the equilibrium dynamic structure factor of the non-driven system. Many-body hydrodynamic interactions and polydispersity in a suspension of particles subject to a constant forcing cause a change of the equilibrium microstructure into a new non-equilibrium state so that the use of a simple Galilei transformation becomes invalid. In electrophoretic experiments, the electro-kinetic coupling of ions and possibly existing electro-osmotic solvent flow are additional complications that add to the complexity in calculating $S(\mathbf{q}, \tau)$.

To rationalize heuristically how the electrophoretic mobility of strongly interacting particles may be determined from a low- q measurement of $G(\mathbf{q}, \tau)$, we make the assumption, just like for non-interacting particles, that diffusion and electrophoretic drift are uncoupled in a weak external field. We impose this assumption on a coarse-grained level only, where distances larger than $\Delta x \gg 2\pi/q_m$ are resolved, corresponding to long correlation times $\tau \gg \tau_m = (q_m^2 D_0)^{-1}$. On ignoring in addition polydispersity effects, the coarse-grained single-particle mean current, $\bar{j}_s(\mathbf{r}, \tau)$, associated with coarse-grained single-particle density $\bar{\rho}_s(\mathbf{r}, \tau)$, can be decomposed as

$$\bar{j}_s(\mathbf{r}, \tau) = -D_s(\phi) \nabla \bar{\rho}_s(\mathbf{r}, \tau) + \mathbf{v}_e(\phi) \bar{\rho}_s(\mathbf{r}, \tau). \quad (53)$$

In this phenomenological description, $D_s(\phi)$ is the unperturbed long-time self-diffusion coefficient, and $\mathbf{v}_e(\phi)$ is identified with the long-time mean electrophoretic velocity of the spheres. In conjunction with the continuity equation,

$$\frac{\partial}{\partial \tau} \bar{\rho}_s(\mathbf{r}, \tau) + \nabla \cdot \bar{j}_s(\mathbf{r}, \tau) = 0, \quad (54)$$

the single-particle eq. (24) is recovered, but $D_s(\phi)$ is replacing now D_0 , and $\mathbf{v}_e(\phi)$ replaces the single-sphere electrophoretic velocity \mathbf{v}_e^0 . The self-intermediate scattering function is here given by

$$G(|\mathbf{q}| \ll q_m, \tau \gg \tau_m) = \langle \bar{\rho}_s(\mathbf{q}, \tau) \bar{\rho}_s(-\mathbf{q}, 0) \rangle \approx \exp\{i \mathbf{q} \cdot \mathbf{v}_e(\phi) \tau\} \exp\{-q^2 D_s(\phi) \tau\}. \quad (55)$$

For deionized aqueous suspensions of PnBAPS68 spheres the system parameters are $\sigma = 68$ nm, $\phi \approx 10^{-3}$, $T = 293.15$ K, $\nu_s(\lambda, T = 20\text{C}) \approx 1.33$ (water), $\lambda = 488$ nm in the static structure factor measurements for zero external field, and $\lambda = 532$ nm in the electrophoresis setup with $|\mathbf{E}| \approx 10 - 120$ V/cm. This gives $\tau_a = a^2/D_0 = 0.18$ ms, $D_0 = 6.3 \mu\text{m}^2/\text{s}$, $(q^*)^2 D_0 = 156$ Hz

corresponding to $\tau_{q^*} = 6.4$ ms, and $q^*/q_m \approx 0.4$ where $q^* = (4\pi\nu_s/\lambda) \sin\{\Theta/2\} = 4.97 \mu\text{m}^{-1}$ is the wave number used in the electrophoretic setup. The correlation times are in the range of 10 – 100 ms or larger so that long-time particle motion is probed.

The assumption on the decoupling of diffusion and drift is flawed when the electric field is so strong that $D_s(\phi)$ and $\mathbf{v}_e(\phi)$ become field-dependent [50]. To test the validity of Eq. (55) in a cell geometry with negligible osmotic flow requires to verify whether the super-heterodyne peaks in $C_{\text{shet}}(\mathbf{q}, \omega)$ are of a Lorentzian shape and, if this has been confirmed, to determine the diffusion coefficient from the measured half-width at half-height, $\Delta\omega_{1/2}$, according to $D_s = \Delta\omega_{1/2}/q^2$. This coefficient should be substantially smaller than D_0 in the case of a deionized system, provided it can be identified with the unperturbed long-time self-diffusion coefficient. The short-time self-diffusion coefficient in these systems, on the other hand, is only slightly smaller than D_0 , with the concentration dependence given by $D_0 (1 - a_t \phi^{4/3})$, where $a_t \approx 2 - 3$ [49].

Finally, to check measured velocities, the electrophoretic mobility is determined by the center of the heterodyne Lorentzian contribution to the power spectrum. It can be compared to theoretical predictions obtained from different methods. Quite recently, substantial progress has been made in developing novel numerical schemes that allow to calculate the electrophoretic mobility of charged colloids at non-zero concentrations. These schemes are based, respectively, on a smoothed surface method, where the sharp colloid-fluid interface is replaced by a diffuse interface [51], on a fluid particle dynamics (FPD) method with charge-densities included [52], and a hybrid simulation method that combines the Lattice Boltzmann fluid description with a Langevin equation treatment of the colloidal particles [53, 54]. A semi-analytic method to compute the electrophoretic mobility, $\mu_e(\phi)$, in dense systems based on a simplified mode-coupling scheme applied to the Primitive Model, has been developed very recently by one of the present authors [55]. All these methods allow, in principle, to explore the electrophoresis of charged colloids with strongly overlapping electric double layers. Also in analytical theory, considerable progress was reported in extending the standard electrokinetic model of dilute systems, and dense systems with weakly overlapping double layers [44, 56] based on the single-macroion cell model, to more dense systems of particles with strong electrostatic interactions [57].

F. Solvent flow profile

The scattering theory described so far assumes a uniform motion of all spheres. This is experimentally realized in cells where the electrodes have a parallel plate capacitor geometry and are placed far away from any container wall to avoid electro-osmotic solvent flow [58]. Cations in solution tend to concentrate at the negatively charged (glass) walls and move towards the cathode, dragging solvent (water) with them. This flow establishes a hydrostatic pressure which tends to force the center of the fluid to flow towards the anode, establishing thus a parabolic back flow in the cell [59]. It is an open question whether the osmotic flow profile is affected significantly by a non-zero concentration of strongly interacting colloidal macro-ions (usually negatively charged) which move towards the anode and drag also solvent along with them. In a first approximation, however, this feedback of the colloids on the fluid flow may be ignored. Moreover, as discussed in [60], to built up an electro-osmotic profile takes quite a large time of the order $0.1 - 1$ s, and this time should be accounted for in experiments with an alternating electric field. In our setup, the switching period is 15 s or larger so that the mobility is measured in the steady-state with a fully developed flow profile.

The electro-osmotic flow profile in the $x - z$ midplane at $y = 0$ of a rectangular vessel, for the solvent streaming along the z -axis with the velocity $u_S(x = \pm d) = u_{eo}$ very near the cell walls, has been calculated by Komagata [36]. On assuming that this profile is macroscopically unperturbed by the interacting colloids, and that the electrophoretic particle velocity, $v_e < 0$, measured relative to the solvent remains constant under the shearing solvent motion, we obtain using Eq. (2),

$$v(x) = v_e + u_S(x) = v_e + u_{eo} \left[1 - 3 \left(\frac{1 - x^2/d^2}{2 - 384/(\pi^5 K)} \right) \right], \quad (56)$$

for the velocity profile of the particles in the laboratory (cell) frame. Here, $K = h/d$, and $\pm d$ and $\pm h$ are the locations of the cell walls in the x and y -direction, respectively. We see here that the solvent profile $u_S(x)$ is proportional to the electro-osmotic velocity, $u_{eo} > 0$, which for small fields grows linearly in E . It is thus characterized by the zero-field mobility, $\mu_{eo} = u_{eo}/|E|$, of microionic cations in the mid-plane close to the cell walls. Again we have assumed equal mobilities and thus equal v_e for all particles. A distribution of velocities can conveniently be introduced at this place, when a coupling of differential velocities and structure is neglected.

In our experiments the aspect K is equal to 10. For the theoretical interpretation of the experimental power spectra of interacting colloids, we assume now that the homogeneous distribution

of particles remains unperturbed by the locally shearing motion of the solvent flow profile so that the particle velocity distribution derives from the Komagata profile according to $P(v) dv \propto n dx$, with n constant. This implies, in turn, that the solvent profile is macroscopically unperturbed by the interacting colloids. The explicit form of the normalized $P(v)$ derived from the Komagata profile is given in [18] and will not be repeated here. In fact, for a sheared suspension of (neutral) rigid colloidal spheres, Brownian motion will give rise to a uniform particle distribution. A flow-induced cross-stream migration is observed, however, for flexible particles like polymers and polyelectrolytes. At large Peclet numbers, this migration can lead to a non-uniform center-of-mass distribution [61, 62, 63].

G. Spectral power for a non-quiet solvent

In making use of the above considerations, we now proceed to a prediction of the power spectrum shape for colloidal particles in an electro-osmotic flow experiment in a closed cell. We follow [18] and use the convolution integral

$$C_{\text{shet}}^M(\mathbf{q}, f) = \int_{v_e+u_S(0)}^{v_e+u_{eo}} dv P(v) C_{\text{shet}}^0(\mathbf{q}, f; v, D_{\text{eff}}), \quad (57)$$

as an approximation to the measured power spectrum $C_{\text{shet}}^M(\mathbf{q}, f)$. Here, $C_{\text{shet}}^0(\mathbf{q}, f)$ is of the form of the single-sphere power spectrum given in Eq. (33), with $f = \omega/(2\pi)$. The integral over the normalized particle velocity distribution function $P(v)$ derived from the Komagata solvent profile extends over a finite velocity range depicted in Fig. 2. The velocity-averaged power spectrum depends also on u_{eo} through its dependence on $P(v)$. Note that (super)-heterodyne scattering is sensitive to particle velocities taken relative to the laboratory (cell) frame.

We summarize here the assumptions underlying Eq. (57): a) the particle electrophoretic velocity is neither coupled to the diffusive motion nor to shear and the stationary parabolic flow profile is unperturbed by the particle interactions (if present); b) the mean particle density remains unperturbed by the shearing motion of the solvent and the applied electric field; c) interaction polydispersity and polydispersity in the electrophoretic velocities are disregarded, and d) density inhomogeneities are not considered irrespective of structure formation in strongly interacting particle systems.

Furthermore we assume e) on exploiting the dominance of incoherent scattering at low q , that the power spectrum of a homogeneous and quiet suspension of strongly interacting colloidal

spheres can be described approximately by the single-particle power spectrum $C_{\text{shet}}^0(\mathbf{q}, f)$ in Eq. (33). Here, we make two replacements. First we substitute D_0 by $D_{\text{eff}}(\phi)$, where in the absence of coupling between diffusion and shear we expect that $D_{\text{eff}}(\phi) = D_s(\phi)$, while at higher shear rates larger values of D_{eff} may be expected [42, 65, 66, 67, 68]. Second, we replace v_e^0 by $v(\phi)$. Likewise, the 'static' prefactor $\langle I_s^0(\mathbf{q}) \rangle$ multiplying the relevant super-heterodyne part in Eq. (33) should be replaced by $\langle I_s(\mathbf{q}) \rangle \propto n f^2(q) [9 s^2 + S(\mathbf{q})]$ for a weakly size-polydisperse system.

The power spectrum predicted by Eq. (57), which is a continuous distribution of velocity shifted Lorentzians, is shown in Fig. 4. It has the typical super-heterodyne form consisting of two symmetrically displaced heterodyne wings at about $\pm \Delta f_B$, where $\Delta f_B = \Delta \omega_B / (2\pi)$, a sharp zero-frequency background term indicated by the two narrow vertical lines, and a central homodyne portion symmetrically distributed around zero frequency and unaffected by the velocity distribution. The form of the particle velocity distribution depicted in Fig. 2 is recognized easily in the shape of the super-heterodyne wings, broadened slightly due to diffusion of the particles. Experimentally, only the positive-frequency heterodyne wing of the symmetric power spectrum is resolved, which includes all the information on the velocity distribution and, thanks to the super-heterodyning, is well separated from the non-interesting homodyne part, and there is no overlap of the symmetrically displaced super-heterodyne wings of the power spectrum.

For the analysis of the experimental power spectra in terms of the theoretical spectrum described by Eq. (57), the latter is fitted to the experimental power spectra data (super-heterodyne

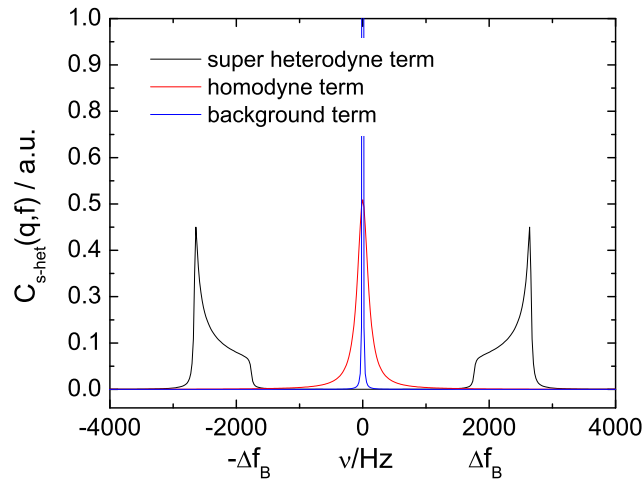


FIG. 4: Theoretically expected power spectrum according to Eq. (57).

wing) using four independent fitting parameters A , v_e , u_{eo} and D_{eff} . Since the overall volume flow in a closed cell is zero so that the mean particle velocity, $\langle v \rangle_P$, is equal to v_e , the position of the center of mass of the heterodyne wing is determined by v_e , whereas the osmotic velocity u_{eo} determines its asymmetric broadening due to the solvent flow, and D_{eff} its symmetric broadening due to the assumed isotropic diffusion. Finally, A is the frequency-integrated part of the power spectrum arising from the positive-frequency super-heterodyne wing. By the sum rule in Eq. (20),

$$A = I_r \langle I_s(\mathbf{q}) \rangle, \quad (58)$$

so that A is determined by the prefactor of the super-heterodyne wing.

IV. EXPERIMENTAL RESULTS

Before analyzing the results of our electrophoretic scattering experiments, we first describe our findings for the field-free static structure factor of deionized systems. Next we discuss our electrophoretic flow experiments starting first with suspensions of non-interacting colloidal spheres and progressing then to fluid-like systems of strongly interacting spheres. Finally, crystalline systems will be shortly addressed.

A. Static light scattering

A standard static light scattering experiment was employed to obtain the measurable static structure factor, $S_M(q)$, from the division of the (background corrected) scattered mean intensity $\langle I_s(q) \rangle - I_s(q)_{\text{H}_2\text{O}}$ of an ordered suspension by the (background corrected) scattered intensity from a non-interacting suspension of the same species (at salt concentration of $c = 4 \times 10^{-4}$ mol/l) weighted with the dilution ratio $n_{\text{non-interacting}}/n_{\text{ordered}}$. The background intensity $I(q)_{\text{H}_2\text{O}}$ of parasitic stray light was determined from measurements of $I(q)$ on the pure solvent. The static structure factor shown in Fig. 5 is for a deionized suspension of PnBAPS68. Experimentally, the pronounced principal peak and the consecutive secondary oscillation are resolved. From a comparison of the signal obtained for the salty suspension to a Rayleigh-Debye-Gans form factor we found an angle-independent background intensity of 0.15 in relative units due to multiple scattering. This offset was subtracted from the static structure factor measured on the deionized suspension. A fit of the experimental structure factor using the decoupling approximation of

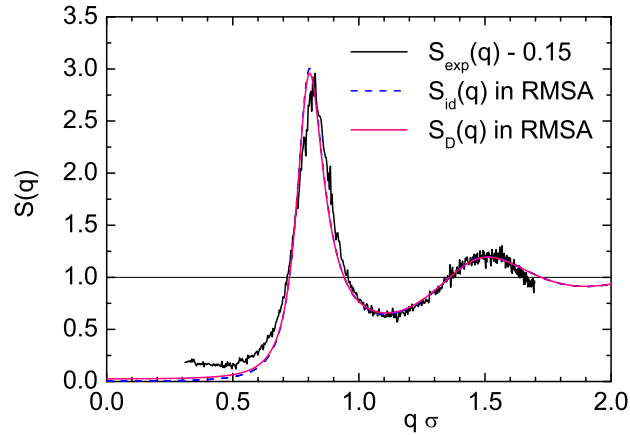


FIG. 5: Experimentally determined static structure factor $S_{exp}(q)$ of a slightly polydisperse, deionized suspension, with $\sigma = 68$ nm, $\phi = 8.38 \times 10^{-4}$, and $s = 0.05$, in comparison to the decoupling approximation structure factor $S_D(q)$, and the structure factor $S_{id}(q)$ of an ideally monodisperse system calculated in RMSA. The effective particle charge has been adjusted to match $S_D(q)$ to the peak height of the experimental $S_{exp}(q)$, by adjusting the effective charge to 575 e. Note that $X(q) \approx 9s^2$ is practically q -independent in the experimental q -range.

Eq. (48) for a polydispersity $s = 0.05$, and an ideally one-component $S(q)$ obtained from the rescaled mean-spherical approximation (RMSA) and a DLVO-type screened Coulomb pair potential, describes the multiple-scattering-corrected data overall quite well. Note that the value of the scattering wave number, q^* , in our super-heterodyne flow experiments is in the low- q region of the structure factor, with $q^*/q_m \approx 0.4$. From the theoretical fit, we have extracted the low- q values of $S_D(q=0) \approx 0.03$, and $S(q=0) \approx 0.0034$, respectively, showing that the incoherent contribution dominates $S_D(q, \tau)$ at very small q . A similar theoretical result is found for the silica particles. In particular for PnBAPS68 the experimental data are above the theoretical expectation, indicating that there is a larger incoherent contribution. Such a contribution is frequently observed in static light scattering and presumably results from optical inhomogeneity of the particles.

B. Electrokinetic flow of non-interacting particles

At a number density of $n = 3.95 \times 10^{16} \text{ m}^{-3}$ ($\phi \approx 3.3 \times 10^{-4}$) and a salt concentration of $c = 5.15 \mu\text{mol/l}$ corresponding to a reduced screening parameter contribution $\kappa_s a \approx 0.97$ a suspension

of Si251 spheres is essentially non-interacting. The measurable static structure factor, $S_M(q)$, in this system is practically equal to one. Fig. 6a shows a series of measured power spectra taken for increasing field strength. The experimentally accessible frequency range is restricted to values in the vicinity of the Bragg frequency of 2 kHz, whose value corresponds to a zero Doppler shift for the super-heterodyne part. Here and in the following figures, the frequency f is taken relative to the Bragg shift, i.e., $f \rightarrow f - \Delta f_B$, so that only the Doppler-shifted frequency is displayed. Near the frequency $f = 0$ corresponding to the Bragg shifted value, the data in Fig. 6 are more noisy and some spectra show additional intensity. This feature is not reproducible and an experimental artefact of still unknown origin. Possibly it stems from stray light reflections containing some low frequency contaminations superimposing with the reference beam. The overall spectral shape, however, clearly reflects the diffusion-convoluted velocity distribution of the heterodyne wing depicted in Fig. 4 and based on Eq. (57). There is a linear shift of the center of mass of the spectra with increasing field strength E , corresponding to an increasing electrophoretic velocity $|v_e| = \mu_e E$. The width of the spectra also broadens, as the electro-osmotic velocity, u_{eo} , near the cell wall increases linearly with the field strength. In addition, there also is a symmetric broadening of the spectra due to isotropic diffusion. These features have been anticipated also in earlier heterodyne dynamic light scattering results [18], but there they have been masked by homodyne contributions and overlap with the complementary 'left-handed' heterodyne wing [18]. With our super-heterodyne setup, these features can be clearly discriminated, allowing thus a fully quantitative evaluation.

Quite interestingly, we find experimentally that the shape of the spectra of non-interacting spheres is given by a single master curve, in accord with the theoretical expectation when $D_{\text{eff}} \propto E$, $\mathbf{v} \propto E$ and $P(v) \propto 1/E$. This can be seen in Fig. 6b where the spectra superimpose on each other when the scaled intensity $C_{\text{shet}}^M(\mathbf{q}, f) \times E$ is plotted versus the scaled frequency f/E . Except for the spurious contributions of low frequency noise near the origin, all spectra coincide nicely within the experimental errors. This shows that the simple superposition of velocity-weighted single-particle Lorentzians used in Eq. (57) works quite well for the considered systems of non-correlated particles, where $S_M(q) \approx 1$. In other words the measured spectra can be directly interpreted as velocity distributions broadened by diffusion-like mechanisms characterized by D_{eff} . This allows us to include a velocity scale, at the top of Fig. 6a by multiplying f with $2\pi/q = 0.796$.

We have fitted all measured spectra by Eq. (57) using the four independently adjustable parameters: v_e , u_{eo} , D_{eff} and integrated scattering signal strength A . The fits describe the experimental

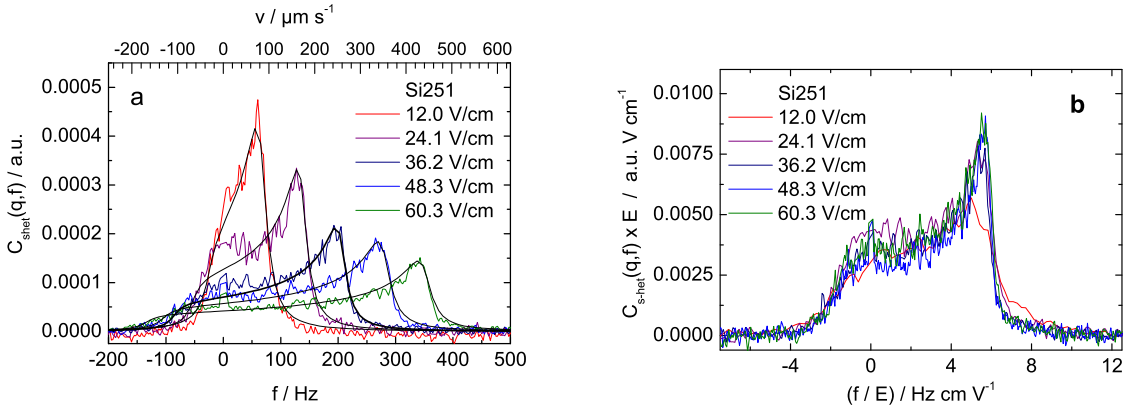


FIG. 6: Power spectra obtained for non-interacting Si251 spheres at a salt concentration of $c = 5.15 \mu\text{mol/l}$ and a number density of $n = 3.95 \times 10^{16} \text{ m}^{-3}$. The frequency is taken relative to the Bragg-shift Δf_B . The smooth solid lines are fits of Eq. 57 to the data. The power spectra are well described in all cases, thus the superposition procedure works well. The upper scale shows the corresponding velocities obtained from $v = 2\pi f/q$. b: scaled spectral power versus reduced frequency. All spectra nicely coincide, showing that in all cases the flow is parabolic.

power spectra of non-interacting particles quite well. This implies, as expected, that the flow profile in these systems is of parabolic shape. The results for the optimized parameters of these fits are included in Figs. 7a-c and compared with the results for suspensions of strongly interacting particles that will be discussed in the following subsection. Both the electrophoretic and electro-osmotic velocities deduced from the fit increase linearly with increasing field strength (see Fig. 7a). This is an important first check, showing that we are in the linear response limit of electrokinetics and that the applied field strength is much smaller than the field within a particle double layer. Our fits further yield $u_{eo} > |v_e|$, corresponding to a strong electro-osmotic shear flow close to the wall.

Furthermore, a roughly field-independent effective diffusion coefficient is obtained for the non-interacting case with $D_{\text{eff}} = 4 \times 10^{-12} \text{ m}^2/\text{s}$. The coefficient has a value somewhat larger than the Stokes-Einstein value $D_0 \approx 1.7 \times 10^{-12} \text{ m}^2/\text{s}$ of the Si251 spheres, and shows the indication of a slight increase with the applied field. A more strongly pronounced and linear increase of D_{eff} with the applied field has been observed in an earlier study on low salt, but non-interacting polystyrene latex suspensions [18], where D_{eff} was found to extrapolate approximately to D_0 in the

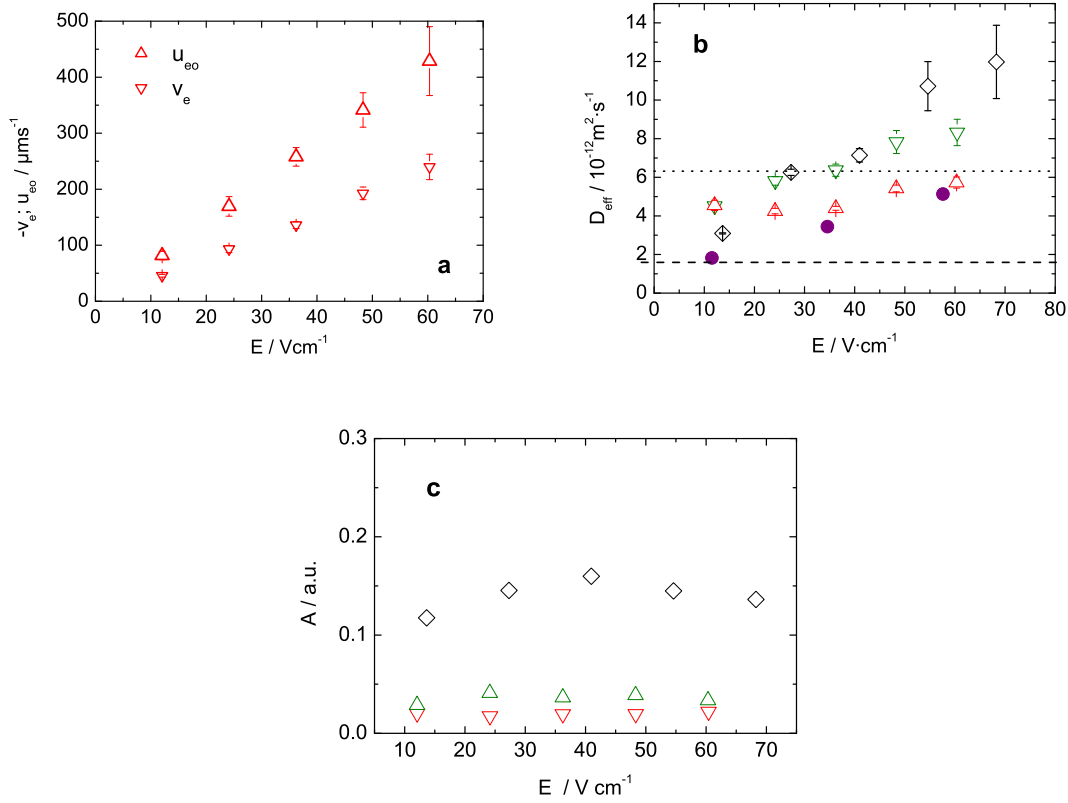


FIG. 7: Fit parameter results in dependence on the applied field strength. a: electrokinetic velocities, $|v_e|$ (down triangles) and u_{eo} (up triangles) for non-interacting Si251 at $n = 3.95 \times 10^{16} \text{m}^{-3}$ and $c = 1.32 \mu\text{mol/l}$; b: comparison of effective diffusion constants, D_{eff} , for the following suspensions: Si251 at $n = 3.95 \times 10^{16} \text{m}^{-3}$ and $c = 5.15 \mu\text{mol/l}$ (up triangles), Si251 at $n = 3.95 \times 10^{16} \text{m}^{-3}$ and $c = 1.32 \mu\text{mol/l}$ (down triangles), Si251 at $n = 3.95 \times 10^{16} \text{m}^{-3}$ and $c = 1.07 \mu\text{mol/l}$ (diamonds) and PnBAPS68 at $n = 0.47 \mu\text{m}^{-3}$ and $c = 0.2 \mu\text{mol/l}$ (closed circles). The two horizontal lines indicate the Stokes-Einstein values $D_0 = 6.30 \times 10^{-12} \text{m}^2/\text{s}$ and $D_0 = 1.71 \times 10^{-12} \text{m}^2/\text{s}$ for PnBAPS68 (dotted) and Si251 (dashed), respectively. c: comparison of integrated spectral intensities A for Si251. Symbols as before. The principal peak of $S(q)$ in the three suspensions takes values of about 1, 1.3 and 1.7, respectively, indicating increasing particle correlations.

zero-field limit. The enlarged value for D_{eff} at small E may have several origins. Most probable, transient time broadening, and/or an increased sample temperature due to Joule heating expected at this elevated salt concentration cause the enlarged D_{eff} . The possible additional increase with increasing field will be discussed in detail below.

The frequency-integrated power spectrum of the non-interacting system is found to be essentially field-independent (up triangles in Fig. 7c). According to Eq. (58), the frequency-integrated intensity of the super-heterodyne wing for non-interacting monodisperse particles is given by $A \propto nP(q)$, where $P(q)$ is the single-sphere form factor. It is independent of the (normalized) particle velocity distribution and D_{eff} . An enlarged E stretches the super-heterodyne wing due to the increased u_{eo} (solvent flow profile becomes more parabolically stretched out), and frequency-shifts its center of mass due to the increased value of v_e , but the frequency-integrated super-heterodyne part, i.e., the 'area' A under the wing, should remain constant unless $P(q)$ or n would change significantly in the presence of a field.

C. Electrokinetic flow of fluid-like suspensions of interacting particles

We now proceed from non-interacting suspensions to systems of increasingly pronounced short-range order and decreasing isothermal osmotic compressibility. Upon reducing the salt concentration at constant $n = 3.95 \times 10^{16} \text{ m}^{-3}$ for Si251, or increasing the particle concentration of deionized ($c = 0.2 \mu\text{mol/l}$) PnBAPS68 spheres from $n = 0.47 \mu\text{m}^{-3}$ to $n = 4.7 \mu\text{m}^{-3}$, the peak heights of the field-free static structure factor have values of 1.3 and 1.7 for Si251, and 2.0 and 2.6 for PnBAPS68. Thus all these samples are in the isotropic fluid state with their short range order becoming more and more pronounced in that order. We first discuss the spectral shapes and then turn to the effective diffusivities and the frequency-integrated power spectrum.

Let us first make a general remark on spectra recorded at moderately strong interactions. According to the sum rule in Eq. (51), $g_E(\mathbf{q}, \tau) \approx |c|^2 N f^2(q) [9s^2 G(\mathbf{q}, \tau) + S(\mathbf{q}, \tau)]$, the IACF is a weighted superposition of coherent and an incoherent part. An expression for the coherent part in an external field is not yet known. Correspondingly, the integrated spectral power in Eq. (58) is given by $A \propto nP(q) [9s^2 + S(\mathbf{q})]$ for slightly size-polydisperse systems and, more generally, by $A \propto n \overline{f^2}(q) S_M(\mathbf{q})$. With increasing interactions the low- q form of $S(\mathbf{q})$ decreases but the incoherent scattering contribution may not yet dominate the coherent one. In such a situation, the major assumption underlying Eq. (52), namely the dominance of the incoherent scattering part, does not necessarily apply. Rather, we expect also the coherent (steady-state) dynamic structure factor, $S(\mathbf{q}, \tau)$, to contribute to the spectrum. And since to date no exact theoretical expression is known for this quantity and its Fourier transform, one should be cautious in interpreting spectra of systems of moderately interacting particles as velocity distributions. On the other hand, any

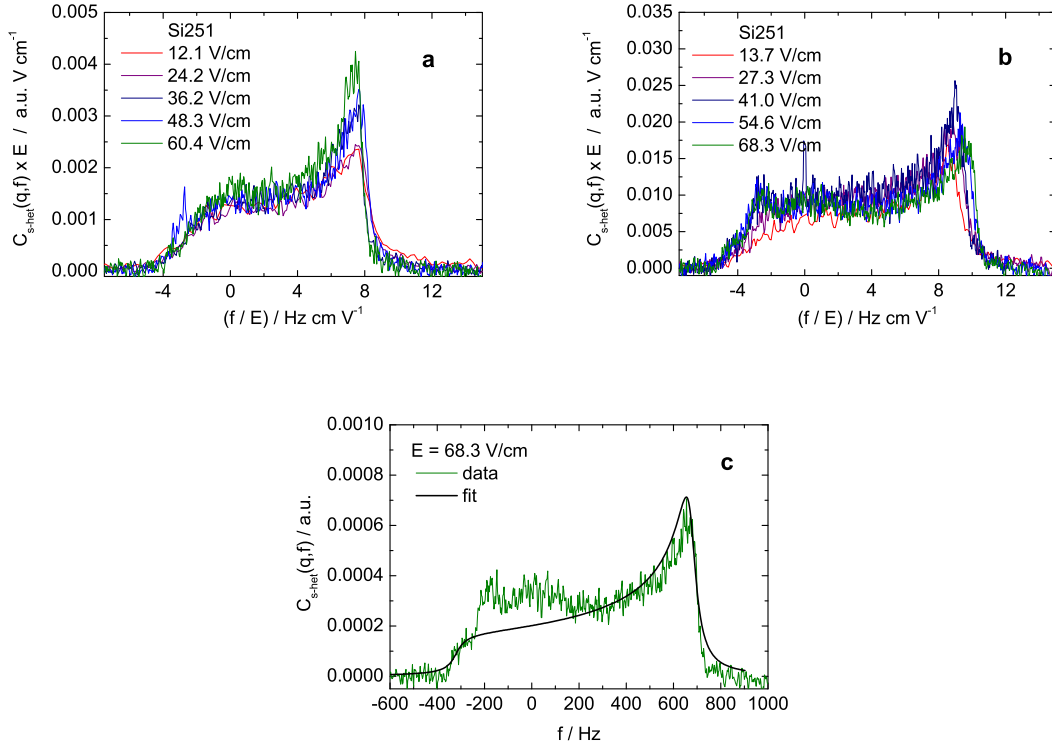


FIG. 8: Suspensions of weakly and moderately strongly correlated particles of Si251 at $n = 3.95 \times 10^{16} \text{ m}^{-3}$. a: field-strength scaled spectra at $c = 1.32 \mu\text{mol/l}$, for field strengths as indicated; b: as in a but for $c = 1.07 \mu\text{mol/l}$; c: comparison of the $E = 68.3 \text{ V/cm}$ spectrum in b: with the fit curve derived from Eq. (57). Note the extra spectral power in the experimental data at moderately small frequencies.

(field-dependent) deviation from the expected spectral shape and amplitude may indicate interesting underlying physics.

In Fig. 8a, we show the field-scaled power spectra for the weakly interacting silica spheres. Again all spectra superimpose neatly. Only minor changes of the spectral shape are observed, mainly appearing as a slight increase in the peak region as the field is increased. In Fig. 8b, five spectra are superimposed for the moderately strongly interacting silica suspension. The field-dependent changes of the spectral shape in Fig. 8b are more pronounced than before. In particular one observes a relative increase of spectral power for the high-shear, low velocity part of the spectra. While this feature is essentially absent at the lowest fields and high-quality fits are obtained, the fits at large fields are considerably worse. This is highlighted in Fig. 8c, where we compare the (unscaled) experimental super-heterodyne signal to a fit of Eq. (57). The difference between ex-

pected and measured spectral power distribution in the interval $-200 \text{ Hz} < f < 200 \text{ Hz}$ is clearly visible. Neglecting this region, a reasonably accurate description of the data is still achieved, compromising between peak intensity and diffusive-like broadening. A fit by Eq. (57) used for is based on the assumption of homogeneously distributed, identical scatterers and a parabolic flow profile. Thus either local changes of scattered intensity or deviations from parabolic flow may cause the deviations observed. The restricted frequency range for the relative enhancement of the experimental spectral power points to a local effect. One possible cause could be shear- or wall-induced changes in $S(\mathbf{q}, \tau)$. In principle, it should be even possible to discriminate between local effects on the scattering power and global changes of the flow profile. To this end we checked for the linearity of the increase in the velocity corresponding to the center of mass of the spectra with increasing field strength. An increased scattering power at low frequencies would indicate a decreased apparent velocity. In contrast to this, a changed flow profile would not be such an indication, since for closed cell boundary conditions the integrated solvent motion must average to zero. In the present case, the observed deviations from a linear increase of the velocity with increasing field was still below the experimental uncertainty in v_e .

In Figs. 9a-b, we show the scaled spectra for low-salinity suspensions of strongly interacting PnBAPS68 spheres. The extension of the spectra in terms of scaled frequency is more narrow than in the spectra considered before, and they start at about zero frequency. The electro-osmotic velocity in this case is much smaller, and on the order of the particle electrophoretic velocity. In turn, this implies a less curved parabolic solvent profile stretching to smaller velocities in the cell center. Interestingly, the low- f overshoot of the experimental power spectrum is absent in these samples. Second, in particular for the more concentrated sample, the overall spectral power increases significantly with the applied field. Still, all these spectra can be fitted rather well using Eq. (57), and Fig. 9c gives an example of the excellent fit quality. The simple superposition procedure in Eq. (57) again works well and the parabolic flow profile is confirmed. Here the reduction of the low- q form of $S(\mathbf{q})$ is sufficient to obtain a super-heterodyne spectrum dominated by incoherently scattered light, in accord with the requirement underlying Eq. (52). Thus, like for the non-interacting case, we again may interpret these spectra as velocity distributions. This main result of the experimental part of our paper on flow measurements is corroborated by the observation that the experimentally determined electrophoretic velocities are in excellent agreement with both state-of-the-art analytical calculations [57], and combined Monte Carlo and Lattice-Boltzmann computer simulations on the Primitive Model level [53, 54].

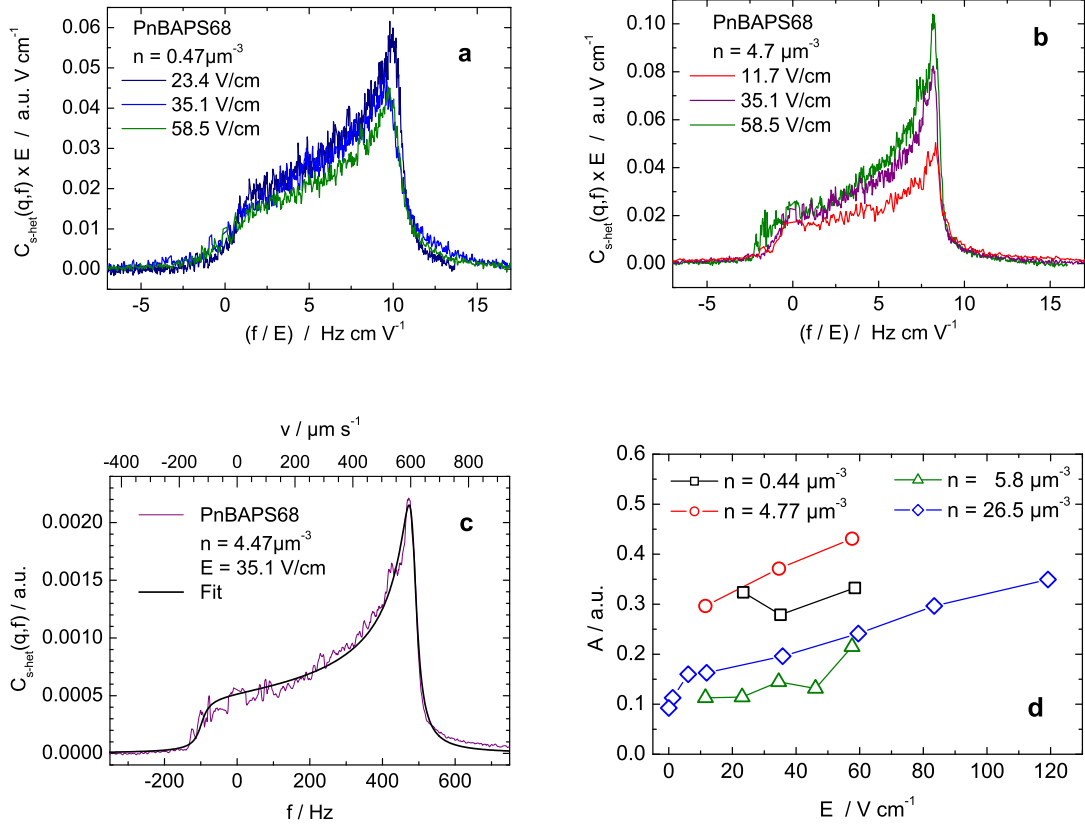


FIG. 9: Fluid-like suspensions of strongly interacting PnBAPS68 particles. a: scaled spectra for PnBAPS68 at $n = 0.47 \mu\text{m}^{-3}$ and $c = 0.2 \mu\text{mol/l}$, for field strengths as indicated; b: scaled spectra at $n = 4.7 \mu\text{m}^{-3}$ and $c = 0.2 \mu\text{mol/l}$ for field strengths as indicated. c: background corrected spectrum for $n = 4.7 \mu\text{m}^{-3}$ and $E = 35.1 \text{V/cm}$, with fit curve according to Eq. (57) d: field-strength dependence of the integrated spectral power for different particle concentrations as indicated.

Given this, a further comparison of the other two fit parameters reveals some interesting deviations which seem to contain information on interesting underlying physics, not yet fully understood. The effective diffusion coefficients, D_{eff} , of the silica systems at different salinities and as a function of increased field were compared in Fig. 7b to those of PnBAPS at $n = 0.47 \text{m}^{-3}$. For the three Si251 samples, the zero-field extrapolated values are above the Stokes-Einstein result (dashed line) with a mild decrease with increasing particle interactions. It is well known that the (equilibrium) long-time self-diffusion coefficient decreases below the Stokes-Einstein value with increasing interactions, whereas the opposite trend appears for the collective diffusion coefficient $D_c = D_0 H(0)/S(0)$ [1]. Our finding therefore nicely illustrates the sum rule in Eq.

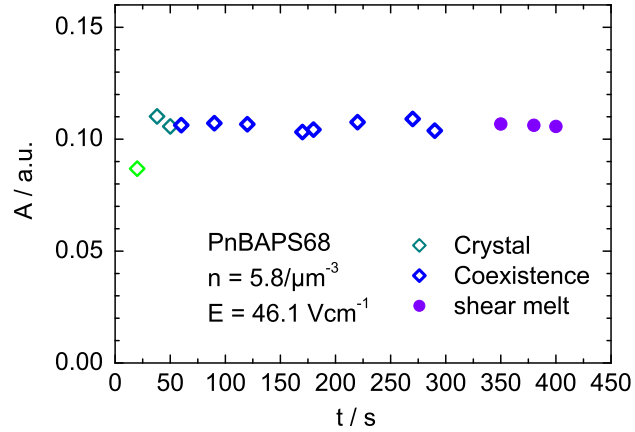


FIG. 10: Integrated spectral power for a shear melting suspension of PnBAPS68 at $n = 5.8 \mu\text{m}^{-3}$. A field of $E = 46.1 \text{ V/cm}$ was applied at $t = 25 \text{ s}$. After the initial jump from its zero-field value, A stays constant irrespective of the system structure

(51), as it shows an originally dominating, but decreasing influence of the coherently scattered light with decreasing isothermal compressibility, which in turn lowers the contribution of collective diffusion. For the deionized suspension of PnBAPS68 spheres, linear extrapolation gives a value $D_{\text{eff}}(E = 0) \approx 1 \times 10^{-12} \text{ m}^2/\text{s}$ well below D_0 (dotted line), and in accord with the expectation for the value of the long-time self-diffusion coefficient. Thus, estimates of the latter quantity may be obtained from extrapolation of $D_{\text{eff}}(E = 0)$ to zero field, but only for strongly interacting fluid systems, where incoherent scattering dominates and additional broadening mechanisms are absent.

Fig. 7b further reveals an increase of the effective diffusion coefficient, D_{eff} , with increasing field strength. The effect is only slightly visible at low n and large salt concentrations, but becomes more pronounced for decreased salinity in Si251, and increased particle number density in PnBAPS68. The field dependence thus increases with increasing interaction strength. Conversely, the approximate theory embodied in Eq. (57) predicts a field strength independent diffusivity, which in fact was observed in the non-interacting case. In the deionized case, Joule heating cannot be responsible for this dependence, as it vanishes with decreasing salt concentration. Transient time broadening, which couples the particle velocity to a non-diffusive peak-broadening, may in

principle play a role, but the experimentally observed broadening is too large for this [18]. In addition, the effect is also pronouncedly present for PnBAPS68 at strong fluid-like order, where the electro-osmotic profile, and thus the absolute velocities are much smaller. We therefore exclude both mechanisms from causing the observed field dependence of the effective diffusion coefficient. A number of possible causes will be discussed at the end of this sub-section.

The field dependence of the integrated spectral power is shown in Fig. 7c for the three silica systems and in Fig. 9d for four differently concentrated suspensions of PnBAPS68. The integrated power for the silica systems does show roughly field independent values, which differ for each suspension. Also for PnBAPS68 each system shows a different overall intensity but here for the more concentrated systems a trend of A to increase with the applied field is obvious. The first observation is traced back to a detail of the experimental procedure. Each system has a different scattering power at low q . This is either due to the different isothermal compressibility (for Si251 at different salinity) or different particle concentration (PnBAPS68). With changing scattering power of the suspension, also the reference beam intensity has been adjusted to obtain an optimized signal-to-noise ratio. This manual adjustment, however, is not precisely defined, leading to differences in A for different suspensions. Hence the absolute values for A should not be compared. For a given suspension, however, the optical adjustment is kept and hence the field dependence can be studied without ambiguity. Therefore the observation of an increased spectral power with increased field strength is an interesting finding, which is possibly connected to the increase of the effective diffusion coefficient with the applied field. Recalling that in general, $A \propto n \overline{f^2}(q) S_M(\mathbf{q})$, a field induced density fluctuation on a suitable length scale will lead to an enlarged value of A with increased field. To pursue this idea, further, we performed a measurement of the frequency-integrated power spectrum as a function of time for a shear-melting suspension of PnBAPS68 at $n = 5.8 \mu\text{m}^{-3}$ with the spectra shown in Fig. 10. The integrated spectral power jumped discontinuously from its zero-field value to a 30% larger value upon application of the field. The fully crystalline state was stable for about half a minute, then the crystal slowly melted inwards and the final stationary state of a shear-molten structure in the mid-plane of the cell was reached after some five minutes. During the whole process, A stayed practically constant. This suggests that the increase of spectral power observed in the field-dependent measurements is not due to a change in the structure. Rather, the initial jump seems to indicate a correlation with the presence of the electric field.

Several previous studies were concerned with the coupling of diffusivity and/or density fluc-

tuations to external fields. Qiu et al. [64] studied the long-time self-diffusion of non- or weakly interacting charged spheres under low frequency, oscillatory Couette flow. With increasing shear, they observed anisotropic self-diffusion, with the mean-squared displacement in the direction of the flow field growing faster than linear in time. This was attributed to Taylor dispersion driven by the position-dependent flow [65]. In addition, a non-convective enhancement of diffusion was found also perpendicular to the flow direction, characterized by a diffusion constant that increases with the shear rate. This shear-induced enhancement of self-diffusion in strongly sheared, dilute suspensions of charged particles was attributed by Breedveld and Levine to the electrostatic breaking of the time reversal symmetry of particle trajectories in low Reynolds number flow [67]. Stokesian dynamics simulations for non-dilute, sheared suspensions of hard spheres also show a pronounced shear-induced enhancement of long-time self-diffusion perpendicular to the flow direction [68]. Conversely, recent analytic calculations and Brownian dynamics simulations (without hydrodynamic interactions) of collective diffusion of hard spheres [42] found the shear-induced change in the collective diffusivity tensor away from isotropy to be quite small at small shear rates (Peclet numbers). Not much is as yet known about suspensions of strongly interacting particles under shear. But, due to the overall parabolic flow profile for fluid-ordered suspensions in the present experiments, we expect an inhomogeneous spatial distribution of observable effects.

In a recent study on the electrokinetics of charged spheres in a quiescent solvent, Araki and Tanaka [52] performed numerical calculations based on a so-called fluid particle dynamics (FPD) method, where the colloidal particles are described as highly viscous liquid spheres and the solvent and microions are treated as continuous fields akin to standard electrokinetic theory. The FPD method accounts for many-particle hydrodynamic interactions. Within the linear response regime of the field-dependence of the electrokinetic velocities, the authors found hydrodynamically induced velocity fluctuations which increased with the field strength. Clearly, such fluctuations will directly mimic an enhanced diffusivity. For low field strengths, the velocity fluctuations decreased monotonically with increasing salinity but at larger field strength the scaled velocity fluctuations pass through a minimum at some intermediate salinity value. The authors further pointed out that these fluctuations significantly alter the pair correlation function, i.e. they translated into density fluctuations. It will be interesting to explore how such fluctuations, which should likewise grow with the electric field, behave on large spatial scales and translate into alterations of the low- q $S(\mathbf{q})$.

Finally, an enlarged apparent diffusivity and corresponding global density fluctuations of non-

hydrodynamic origin, can be expected when fluctuations in relative particle velocities are caused by a non-negligible mobility polydispersity. Here particles move at different constant speeds which introduces a broadening of the velocity distribution. Similar to hydrodynamic broadening, this effect is independent of the absolute particle velocity but proportional to the relative velocity between neighboring particles i and j which will increase with the applied field: $\Delta v = (\mu_i - \mu_j)E$. In the former case the effective diffusivity is enhanced, in the latter the velocity distribution is convoluted with the mobility distribution (e.g., of Gaussian shape for a narrow distribution). As both types of independent spectral broadening mechanisms cannot be discriminated properly within the spectra, polydispersity of mobilities may mimic an increased diffusion. On the other hand, also the suspension microstructure is likely to be affected by the systematic differential motion of neighboring particles. If density fluctuations occur at the appropriate scale, the relative amplitude of the coherent scattering contribution would be enhanced. This spatially global effect should become stronger with increasing field strength, but could also decrease with increasing particle interactions, as the isothermal osmotic compressibility decreases and the structural ordering becomes more pronounced. A discrimination between all these possibilities may be attempted by applying our method to different flow situations, with particular focus on those, where the external field couples differently to particles, micro-ions and solvent.

D. Electrokinetic flow of crystalline systems

In this last subsection, we shortly address crystalline systems as formed in deionized suspensions of PnBAPS68. In this case, the finite shear moduli and the different viscosities of the different phases coexisting under shear cause deviations from a parabolic flow profile [31, 32, 33]. We therefore expect that Eq. (57) cannot be used. In fact, the shape of the power spectrum in the crystalline state at low electric field strengths is quite different to that of the stationary state at large fields, where the systems shear melts within a few minutes. This is seen for the lowest applied field strength in Fig. 11a, for PnBAPS68 at a particle density of $n = 5.8 \mu\text{m}^{-3}$. A qualitative estimate of the flow behavior was obtained from microscopy. At low field strength E , one observes some kind of double plug flow, lubricated by a layer crystal region. At a value $E = 22.05$ V/cm, the layer crystal fills the complete cell and the flow profile takes a parabola-like shape. At $E = 34.6$ V/cm and larger, the system is shear-molten at mid-cell height. The system of Fig. 10b is at $n = 26.5 \mu\text{m}^{-3}$ and stays fully crystalline even at the largest applied field strength. Micro-

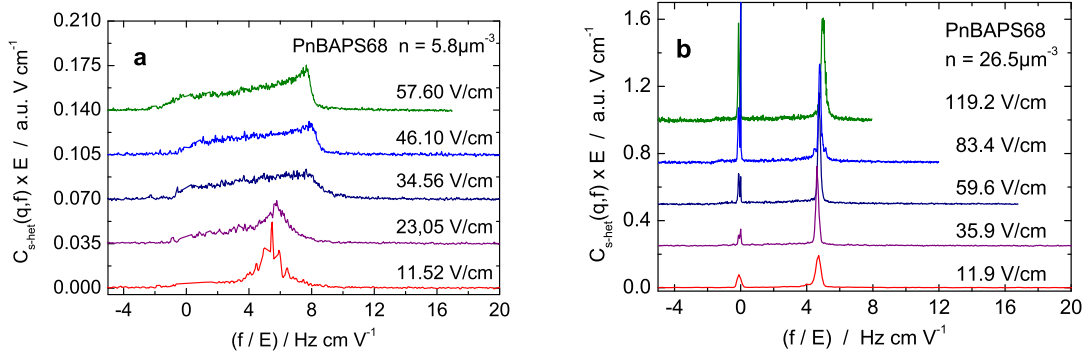


FIG. 11: Scaled power spectra for two equilibrium crystalline suspensions of PnBAPS68. Spectra are shifted upward for clarity. a: $n = 5.8 \mu\text{m}^{-3}$. With increasing field strength this system consecutively shows double plug flow, layer crystal plastic flow and complete shear melting; b: $n = 26.5 \mu\text{m}^{-3}$. With increasing field strength this system shows double plug flow but no shear melting. All flow profiles, even those in the shear molten state, deviate strongly from the parabolic flow profile entering into Eq. (57).

scopic observation here reveals a double plug flow in opposing directions. The directly observed flow behavior is mirrored in the spectral shapes, and none of these spectra can be fitted well by a parabolic flow profile according to Eq. (57). Interestingly, this applied also to the systems which were completely shear-molten at mid-cell height. Height dependent measurements show that this is due to an incomplete shear melting in y -direction, altering thus the aspect.

Clearly, the homogeneity assumption used in the derivation of the scattering theory is valid only locally in (partially) crystalline systems. and invalidated at each slip line and/or phase boundary, while at the same time the long time self-diffusion coefficients are expected to differ considerably for different suspension structures [69]. Therefore, Eq. (57) has to be applied with great caution in both integral and local measurements. For the low diffusivity case of crystalline or partially shear-molten states under hydrostatically induced flow through a capillary, the comparison of local and integral spectra, however, suggests that in a qualitative way the latter can still be interpreted as velocity distributions and estimates, e.g., of the electrokinetic velocities be obtained [33]. Moreover, Fig. 10 has shown that the spectral power does not change upon changing the suspension structure. This allows further quantitative evaluation of flow profiles, as the intensity at a given frequency is then proportional to the number of scatterers moving with the corresponding velocity. Hence, within the uncertainty of unknown but presumably small diffusional broadening, quite complex flow profiles should be analyzable at least on a qualitative level. In fact, flow profiles con-

sistent with theoretical expectations for multiphase flow have been extracted from point-by-point measurements of local velocities in pipe flows under hydrostatic pressure differences [28, 29].

V. CONCLUSIONS

Integral heterodyne velocimetry is an established method to measure flow in colloidal systems. It was applied in the past both in electrokinetic and rheologic contexts to study electrophoretic mobilities and multi-phase flow, and the theoretical expressions derived for non-interacting suspensions were applied to estimate velocity distributions and flow profiles. In the present paper, we went beyond this ad-hoc ansatz and extended the experimental method to super-heterodyning. Moreover, we could complement this by a derivation of a theoretical expression accounting for structure formation and the unavoidable polydispersity of real colloidal systems and a careful discussion of the performance and scope of this approximate approach. Our analysis shows that for small size polydispersity and sufficiently low isothermal compressibility (more precisely: low- q coherent scattering intensity) of the suspension, the signal in the low- q limit should be dominated by incoherent scattering. Experimentally, a low compressibility was realized by using strongly interacting low-salt suspensions, in the fluid or crystalline state. In our theoretical considerations, we first assumed a constant particle electrophoretic velocity and a homogeneous suspension. Experimentally, we studied electrokinetic flow in closed cells yielding parabolic flow profiles. Spatial variations of the velocity were theoretically accounted for by convoluting a theoretical expression for the particle velocity distribution with the single-velocity spectral power form. In this way, we obtained an excellent description of the measured power spectra for fluid-ordered systems.

Under the assumptions made in the scattering theory presented here, the derived expression for the incoherent spectra is identical in form, but not in value, to that of the non-interacting case. It can be fitted to experimental spectra using four independent parameters of which two (effective diffusion coefficient and integrated spectral power) are disregarded in the further evaluation for the electrokinetic velocities. This neglect works well even in the case of crystals and of field-induced structural changes [26, 27, 28]. The electrophoretic mobility for shear-melting systems was found to be constant, irrespective of the applied field strength and the stationary system microstructure. This finding is fully consistent with recent simulations including hydrodynamic interactions [54]. So there already is a practical assessment of this approach for the complicated case of electrokinetic flow and shear. Inclusion of different experimental situations, like hydrostatic tube flow,

Couette-shear, sedimentation, and even shear-banding flows appears to be rather straightforward. Hence the presented method promises to become a valuable tool in the studies of colloidal dispersions under flow.

A deeper theoretical understanding, however, remains as a challenge, to be addressed in future work. In particular, the observed dependencies of the effective diffusion coefficient and the spectral power underline the importance of fluctuations, which have not been considered so far in the above mentioned evaluations but should be included in our simple theoretical model. Irrespective of their origin (shear-induced Taylor dispersion, hydrodynamic coupling by micro-ion currents, polydispersity in the electrokinetic mobility or sedimentation velocity), it is reasonable to expect that differential motion of neighboring particles will affect the suspension microstructure and may couple to density fluctuations on the scale of nearest neighbors distances and larger. So in all these cases, we expect an enhanced contribution of coherent scattering to the spectra. In particular, an extension of the theoretical treatment to the coherent dynamic structure factor, $S(\mathbf{q}, \tau)$, is highly desired, which also includes a worked-out calculation of its self-part $G(\mathbf{q}, \tau)$. This should also include strongly interacting suspensions with fully developed fluid microstructure and polydispersity effects. This, of course is quite demanding, since there is no general expression available to date for the steady-state dynamic structure factor $S(\mathbf{q}, t)$ in driven systems covering all cases of driving fields ranging from simple shear over sedimentation, where we have a relative motion of colloidal particles against the backflowing solvent, to electrokinetic motion which combines shear flow with particle motion against the solvent. In all three cases the coupling between structure and diffusivity via direct interactions and hydrodynamic interactions is different, and in any case very complex. A practical aid in this task could again be given by the experiment, by comparing angle-dependent measurements in the three different situations. This could clarify whether the changes in the power spectrum are caused by the particle motion relative to the solvent, the shear flow or the applied electric field. Special interest may further be given to the flow forms in binary mixtures of low-polydispersity samples. By a suitable choice of particle material, size and charge, each of the mentioned external perturbations may act differently on the two species and induce clearly separated signatures in the spectra.

The present paper has reported on an important methodical development, both from the experimental and theoretical points of view. It sets the stage for progressing from the quantitative characterization of flow in terms of transport coefficients to a deepened and more general understanding of the complex interplay between particle interactions, microstructure and dynamics

under flow.

Acknowledgements

It is a pleasure to thank Nina Lorenz for providing the static structure factor measurements, and Wolfgang Paul and Mathieu McPhie for helpful discussions. Financial support of the DFG (SFB TR6, project sections B1 and B2), and the MWFZ, Mainz is gratefully acknowledged.

-
- [1] P. N. Pusey in J. P. Hansen, D. Levesque, J. Zinn-Justin: *Liquids, freezing and glass transition*, 51st summer school in Theoretical Physics, Les Houches (F) 1989, Elsevier, Amsterdam 1991, pp 763.
 - [2] G. Nägele, *Phys. Reports* **272**, 217 (1996).
 - [3] H. Löwen: *Phys. Reports* **237**, 249 (1994).
 - [4] B. J. Ackerson, *Physica A* **128**, 221 (1983).
 - [5] L. B. Chen, C. F. Zukoski, *Phys. Rev. Lett.* **65**, 44 (1990).
 - [6] J. F. Berret, D. C. Roux, G. Porte, *J. Phys. II (France)* **4**, 1261 (1994).
 - [7] J. K. G.Dhont, M. P. Lettinga, Z. Dogic, T. A. J. Lenstra, H. Wang, S. Rathgeber, P. Carletto, L. Willner, H. Frielinghaus, P. Lindner, *Proc. Roy. Chem. Soc. Faraday Disc.* **123**, 157 (2003).
 - [8] R. Biehl, T. Palberg, *Europhys. Lett.* **66**, 291 (2004).
 - [9] B. J. Ackerson (ed.), *Phase Transitions* **21** (2-4), 73 - 249 (1990).
 - [10] H. Löwen, *J. Phys.: Condens. Matter* **13**, R415 (2001).
 - [11] R. J. Adrian, *Ann. Rev. Fluid Mech.* **23** 261 (1991).
 - [12] M. Atlana, M. Gross, *Rev. Sci. Inst.* **77** 116103 (2006).
 - [13] D. H. Barnhart, R. J. Adrian, G. C. Papen, *Appl. Opt.* **33**, 7159 (1994).
 - [14] J. O. Sherer, L. P. Bernal, *Appl. Opt.* **36**, 9309 (1997).
 - [15] M. D. Alaimo, D. Magatti, F. Ferri, M. A. C. Potenzaa, *Appl. Phys. Lett.* **88**, 191101 (2006).
 - [16] W. van Megen, S. M. Underwood, J. Miller, T. C. Mortensen, S. I. Henderson, J. L. Harland, P. Francis, *Prog. Theo Phys. Suppl.* **126**, 171 (1997).
 - [17] R. J. Adrian (Ed.) *Selected papers on Laser Doppler velocimetry SPIE Milestone Series* Vol. **78** 1993.
 - [18] T. Palberg, H. Versmold, *J. Phys. Chem.* **93**, 5296 (1989).

- [19] J. F. Miller, K. Schätzel, B. Vincent, *J. Colloid Interface Sci.* **143**, 532 (1991).
- [20] K. Schätzel, J. Merz, *J. Chem. Phys.* **81**, 2482 (1984).
- [21] T. Palberg, M. Würth, *J. Phys I (France)* **6**; 237 (1996).
- [22] B. J. Berne, R. Pecora, *Dynamic light scattering*, Krieger, Malabar, Florida ² 1990, pp.53
- [23] J.K.G. Dhont, *An introduction to the dynamics of colloids*, Elsevier, Amsterdam 1996.
- [24] B.R. Ware, *Adv. Coll. Interface Sci.* **4**, 1 (1974).
- [25] H.Z. Cummins, F.D. Carlson, T.J. Herbert and G. Woods, *Biophys. J.* **9**, 518 (1969).
- [26] J.F. Miller, *J. Colloid Interface Sci.* **153**, 266 (1992).
- [27] J. Bergenholtz, N. J. Wagner, *Physica A* **235**, 34 (1997).
- [28] S. v. Hünerbein, M. Würth, T. Palberg, *Prog. Colloid Polym. Sci.* **100**, 241 (1996).
- [29] T. Preis, R. Biehl, T. Palberg, *Prog. Colloid Polym. Sci.* **108**, 129 (1998).
- [30] J. Dzubiella, G. P. Hoffmann, and H. Löwen, *Phys. Rev. E* **65**, 021402 (2002).
- [31] M. Medebach, T. Palberg, *Colloid Surf. A* **222**, 175 (2003).
- [32] M. Medebach, T. Palberg, *J. Chem. Phys.* **119**, 3360 (2003).
- [33] M. Medebach, T. Palberg, *J. Phys. Condens. Matter* **16**, 5653 (2004).
- [34] M. Medebach, L. Shapran, T. Palberg, *Colloid Surfaces B* **56**, 210 (2007).
- [35] H. Reiber, T. Köller, T. Palberg, F. Carrique, E. Ruiz-Reina, and R. Piazza, *J. Colloid Interface Sci.* **309**, 315 (2007).
- [36] S. Komagata, *Researches Electrotech. Lab. Tokyo Comm.* **348**, 1 (1933).
- [37] T. Palberg, W. Härtl, U. Wittig, H. Versmold, M. Würth, E. Simnacher, *J. Phys. Chem.* **96**, 8180 (1992).
- [38] P. Wette, H.-J. Schöpe, R. Biehl, T. Palberg, *J. Chem. Phys.* **114**, 7556 (2001).
- [39] D. Hessinger, M. Evers, T. Palberg, *Phys. Rev. E* **61**, 5493 (2000).
- [40] B. Chu, *Laser Light Scattering: Basic Principles and Practice* (Academic Press, London, 1999).
- [41] H. Furukuwa and S. Hirotsu, *J. Phys. Soc. Japan* **71**, 2873 (2002).
- [42] A. M. Leshansky, J. F. Morris, J. F. Brady, *J. Fluid Mech.* **597**, 305 (2008).
- [43] R.J. Hunter, *Foundations of Colloid Science: II* (Oxford Science Publications, Clarendon Press, Oxford, 1989).
- [44] H. Ohshima, *Theory of Colloid and Interfacial Electric Phenomena* (Elsevier, Amsterdam, 2006).
- [45] M. Lozada-Cassou, E. Gonzales-Tovar, *J. Colloid Interface Sci.* **239**, 285 (2001).
- [46] S.A. Allison, D.A. Stigter, *Biophys. J.* **78**, 121 (2000).

- [47] D. Long, A. Ajdari, *Eur. Phys. J. E* **4**, 29 (2001).
- [48] B. Robertson, *J. Chem. Phys.* **95**, 3873 (1991).
- [49] A. J. Banchio, G. Nägele, *J. Chem. Phys.* **128**, 104903 (2008).
- [50] S. Barany, F. Madai, V. Shilov, *Progr Colloid Polym Sci* **128**, 14 (2004).
- [51] K. Kim, Y. Nakayama, R. Yamamoto, *Phys. Rev. Lett.* **96**, 208302 (2006).
- [52] H. Araki, H. Tanaka, *Europhys. Lett.* **82**, 18004 (2006).
- [53] V. Lobaskin, B. Dünweg, C. Holm, *J. Phys.: Condens. Matter* **16**, S4063 (2004).
- [54] V. Lobaskin, B. Dünweg, C. Holm, M. Medebach, T. Palberg, *Phys. Rev. Lett.* **98**, 176105 (2007).
- [55] M.G. McPhie, G. Nägele, to be submitted.
- [56] S. Levine, G.H. Neale, *J. Colloid Interface Sci.* **47**, 520 (1974).
- [57] F. Carrique, F. J. Arroyo, M. L. Jimnez, A. V. Delgado, *J. Phys. Chem B* **107**, 3199 (2003).
- [58] E. E. Uzgiris, *Prog. Surf. Sci.* **10**, 53 (1981).
- [59] R.J. Hunter, *Zeta-potential in colloidal science: Principles and Application*, Academic, London 1981.
- [60] M. Minor, A.J. van der Linde, H.P. van Leeuwen, J. Lyklema, *J. Colloid Interface Sci.* **189**, 370 (1997).
- [61] R. Khare, M.D. Graham, J.J. de Pablo, *Phys. Rev. Lett.* **96**, 224505 (2006).
- [62] O. Berk Usta, J.E. Butler, A.J.C. Ladd, *Phys. Rev. Lett.* **98**, 098301 (2007).
- [63] L. Cannavacciuolo, R.G. Winkler, G. Gompper, submitted.
- [64] X. Qiu, H. Daniel-Ou-Yang, D. J. Pine, P. M. Chaikin, *Phys. Rev. Lett.* **61**, 2554 (1988).
- [65] G. I. Taylor, *Proc. Roy. Soc. London A* **219**, 186 (1954) and 223, 446 (1954).
- [66] A.V. Indrani, S. Ramaswamy, *Phys. Rev. E* **52**, 6492 (1995).
- [67] V. Breedveld, A.J. Levine, *Soft Materials*, Vol. 1, No. 2, 235-244 (2003).
- [68] D. R. Foss, J. F. Brady, *J. Fluid Mech.* **401**, 243 (1999).
- [69] R. Simon, T. Palberg, P. Leiderer, *J. Chem. Phys.* **99**, 3030 (1993).